Study on an Objective Performance Measure for Spaceborne Wind Sensors

(Figure of Merit - FoM)

ESTEC contract No. 18041/04/NL/AR

KNMI progress report - 2

(January 2006)

Table of Contents

1 Introduction

Wind information over the oceans is available from various sources, e.g., in-situ measurements by ships and buoys, analysis from numerical weather prediction models, and remotely sensed by passive and active microwave spaceborne sensors. It is important to consider the different spatial and temporal sampling characteristics as well as the different error statistics when comparing wind data from these sources. In addition, the error analysis for wind data derived from spaceborne sensors require special care due to non-linearities and ambiguities in the geophysical model functions (GMF) leading to multiple solutions in the wind retrieval.

In order to compare the performance of different spaceborne wind sensors the following error sources have to be considered:

1. The spatial wind variability within the resolution cell adds the so-called geophysical noise due to the non-uniform spatial averaging, inherent in the radar measurement.

2. The physical measurement error is defined by the technical properties of the instrument.

3. The error of the GMF is a not well known function of wind speed and direction, or ancillary geophysical or resolution parameters.

4. The applied retrieval method introduces another error, which might depend to first order on the way of normalization.

5. The number of solutions and their distribution can also be treated as an error.

All these errors contribute to the difference between the true and observed wind, which is at first order a measure of the instrument performance.

The definition of an objective measure of the quality of the wind retrieval has already been studied within the framework of the ESA-ESTEC work on *"Optimisation of Rotating, Range-Gated Fanbeam Scatterometer for Wind Retrieval"* (ESA Contract 14383/00/NL/DC), denoted RFSCAT study in the following. The concept of a figure of merit (FoM) was used, which accounted for the differences between retrieved wind vector and the reference wind as well as the number and distribution of multiple solutions. Problems arose when comparing RFSCAT simulations with *real world data* from existing systems like those on ERS and QuikSCAT. The true wind field is not known for these measurements. Consequently, different error statistics of the reference wind fields as well as different retrieval techniques hampered a fair comparison of the performances of the various systems. However, the FoM concept was well suited for comparing different RFSCAT systems.

The RFSCAT study clearly showed, that the difference between the true and observed wind again is a function of position across the swath and of wind speed. The definition of the FoM, which accounts for these dependencies, will be revisited in this study. Furthermore, the following tasks related to the error sources are foreseen:

Point 1: In the RFSCAT study the spatial sub-footprint backscatter variability was controlled/set to a portion of the mean wind speed. In the proposed study the dependence of the geophysical noise on instrument resolution, wind speed, and GMF will be evaluated in the form of a sensitivity analysis. The result is very important for the comparison of instruments with different footprint sizes and for the comparison of simulations and *real world data*. For the latter comparison data from ERS, NSCAT, and SeaWinds (QuikSCAT/Midori-2) will be used together with simulations of ASCAT.

Point 2: The measurement errors of the systems will be computed and be used in the analysis.

Point 3: The error of the GMF is not know, however for a fair comparison of the systems it has to be assumed that it is eventually of the same order for all instruments.

Point 4: It is proposed to conduct an in-depth analysis of the impact of the retrieval technique. It is known that different retrieval schemes using normalization by measurement *Kp*, solution *Kp*, or no normalisation lead to different error distributions with respect to measurement geometry and wind speed. The analysis will make use of the RFSCAT simulator.

Point 5: The treatment of the number of solutions and their distribution was a major point of concern in the RFSCAT study. The approach of the maximum likelihood estimator (MLE) used in the RFSCAT study will be compared to a description, which is based on the probability of the solutions.

2 Database

A database of collocated wind and radar measurements is needed for the verification of the geophysical noise model as well as for a comparison of real instruments with simulations. Task 1 of this study consists of generating a database of ERS, NSCAT, and SeaWinds (QuikSCAT/Midori-2) data collocated together with wind fields from meteorological reanalysis.

KNMI co-ordinates the scatterometer wind products of the EUMETSAT-sponsored Ocean and Sea Ice Satellite Application Facility (SAF), Climate Monitoring SAF, and the Numerical Weather Prediction (NWP) SAF. In the framework of the mentioned SAFs, KNMI has developed a scatterometer data processing package, which include the generation of operational wind products notably for ERS and SeaWinds systems. Among the useful ad-hoc tools of such package, there is a collocation software, which makes the generation of the database a straightforward task.

At KNMI, the scatterometer team has produced a large collocated dataset of scatterometer and European Centre for Medium-range Weather Forecast (ECMWF) reanalysis data, both for ERS and SeaWinds instruments. The work presented in this report has been performed with one month (January 1993) of such collocations.

3 Preparation for Wind Retrieval

In remote sensing, the relationship between any observation or set of observations and one or more geophysical state variables is generally represented with the following equation:

$$\mathbf{y} = K_n(\mathbf{x}) \tag{3.1}$$

Where **y** is the vector of observations, **x** is the vector of state variables that **y** depends on, and the operator K_n is the so-called forward model, which relates the state variables to the observations; the subscript *n* reminds us that it might be non-linear. The process of deriving the best estimate of **x** for a given **y**, allowing for observation errors, is called inversion. In scatterometry, **x** corresponds to the sea-surface wind vector and **y** to the radar backscatter measurements (σ^o).

The most general approach used for inverting winds from scatterometer measurements is the Bayesian approach. From the Bayes' theorem, we can state that the probability of having a "true" wind given a set of backscatter measurements is proportional to the probability of having a set of backscatter measurements given the "true" wind, multiplied by the prior wind probability:

$$P(\sigma_s^o \left| \sigma_m^o \right.) = P(\sigma_m^o \left| \sigma_s^o \right.) \cdot P(\sigma_s^o) \tag{3.2}$$

where $\sigma_m{}^o$ is the set of backscatter measurements and $\sigma_s{}^o$ is the representation of the "true" wind in σ^o space. As such, by formulating Bayes in σ^o space (see equation 3.2), *Stoffelen* (1998) interprets the prior wind probability as the a priori probability density of having a "true" set of measurements ($\sigma_s{}^o$) somewhere in the multidimensional σ^o space, i.e., $p(\sigma_s{}^o)$.

Based on equation 3.2, a common way of inversion consists of minimizing the following maximum likelihood estimator (MLE) for varying wind speed and direction (*Graham et al., 1989; JPL, 2001*):

$$MLE = \frac{1}{N}\sum_{i=1}^{N}\left(\frac{\sigma_{mi}^o - \sigma_{si}^o}{Kp(\sigma_{Ni}^o)}\right)^2 \tag{3.3}$$

Where N is the number of measurements, $\sigma_{mi}{}^o$ is the backscatter measurement, $\sigma_{si}{}^o$ is the backscatter simulated through the Geophysical Model Function (GMF) for different wind speed and direction trial values, and $\sigma_{Ni}{}^o$ is usually taken to be either $\sigma_{mi}{}^o$ or $\sigma_{si}{}^o$. Here, $Kp(\sigma_{Ni}{}^o)$ is the observation error (noise) and has the form of Kp_i x $\sigma_{Ni}{}^o$, where Kp_i is a dimensionless value which is represented (for any given measurement) in the following way:

$$Kp = \sqrt{Kp_{geoph}^2 + Kp_{instr}^2} \tag{3.4}$$

Where Kp_{geoph} is the so-called geophysical noise, i.e. noise caused by the spatial wind variability within the resolution cell (footprint) and the non-uniform spatial averaging inherent in the radar

measurement, and Kp_{instr} is the instrument noise, i.e. noise produced by the technical properties of the radar. Note that equation 3.4 should also include a GMF error term. Given many measurements, the GMF error is represented by the misfit between the measurements and the GMF. However the misfit is small (and shows no systematic effect at any particular speed, incidence angle or direction regime) compared to K_{geoph} and Kp_{instr} and therefore neglected in equation 3.4. [Note: strictly speaking, when assuming Gaussian errors, a term $\ln(Kp(\sigma^{o}_{Ni}))$ should be added to the right-hand side of equation 3.3 but this term is not significant and, as such, is not used].

As discussed in chapter 2 of *Portabella* (2002), the MLE formulation (equation 3.3) is derived from the use of the Bayesian approach (equation 3.2) with the following set of assumptions:

- measurements are uncorrelated,
- their errors are Gaussian, and
- the a priori probability $p(\sigma_s^o)$ is constant.

The approximation of constant $p(\sigma_s^o)$ is problematic in scatterometry. However, for NSCAT and SeaWinds, the use of equation 3.3 gives useful results in terms of wind retrieval accuracy. This is not the case for ERS, where *Stoffelen* (1998) showed that by transforming the measurement space and removing the noise normalization from equation 3.3, the assumption of constant $p(\sigma_s^o)$ becomes practicable and the wind retrieval is improved.

However, *Stoffelen* (1998) used only instrument noise (a constant value of 0.05) in the measurement noise (equation 3.4) to show that $p(\sigma_s^o)$ is far from constant. No attempt was done at that time to test the geophysical noise model for ERS wind retrieval. Therefore, we first analyse in detail the noise properties of the system and check whether the inclusion of a more realistic *Kp* in equation 3.3 makes the assumption of constant $p(\sigma_s^o)$ valid and, consequently, improves the wind retrieval on the basis of equation 3.3 for ERS.

Moreover, in order to determine an objective performance measure for the different scatterometer systems, it is important to set a generic wind retrieval method. As such, it makes sense to first check whether a unique form of equation 3.3 can be used for all scatterometer systems.

3.1 ERS case

3.1.1 Determination of geophysical noise parameters

As mentioned before, we presume that the geophysical noise is caused by the sub-footprint spatial wind variability and the non-uniform spatial sampling of backscatter measurements. In particular, for ERS, several sub-cell resolution σ^o measurements are averaged to produce a single σ^o measurement for every beam (i.e., fore, mid, and aft). These sub-cells are centered in different locations of the footprint and as such observe somewhat different winds due to wind variability.

Therefore, the geophysical noise will depend on both the sub-footprint wind variability and the number of independent σ° samples. [Note: both the number of independent samples and the wind variability are determined by the sub-cell resolution]. In fact the geophysical noise depends on the ratio between the wind variability and the square root of the number of samples. That is, both parameters have a similar effect on the geophysical noise, but with opposing tendencies.

In order to derive the geophysical noise, a simulation of the backscatter triplets (fore, mid, aft) is performed and compared to real triplets. In the simulation, we assume as input a true wind Gaussian distribution centered at 0 m/s with a standard deviation (SD) of 6 m/s in the wind components. Then, for each input wind vector we can simulate the triplets using the CMOD-5 GMF (*Hersbach, 2003*) for different values of wind variability and σ° samples. In practice, since the two parameters have a similar effect, one of them, i.e., the sampling number, is set to a fixed value. A realistic instrument noise value per beam and WVC number[1] is used in the simulation.

For a given scatterometer, its set of N σ° measurements defines a GMF surface in a N-dimensional σ° space for varying speed and direction. For the ERS triplet ($\sigma_1^\circ, \sigma_2^\circ, \sigma_3^\circ$), this surface has the shape of a cone in the 3D space (see chapter II of *Stoffelen, 1998*). Figure 3.1 shows the real and simulated triplets that belong to a particular section of the cone (for analysis purposes, the section has a certain thickness in order to allow a significant amount of triplets in the plot). Both CMOD-4 (*Stoffelen and Anderson, 1997b*) and CMOD-5 GMF cone sections are also shown. The uppermost triplets correspond to winds blowing along the mid beam (upwind/downwind), whereas at the lowest points the wind blows roughly across the mid beam (crosswind).

Figure 3.1a shows that most of the real triplets are located in the inner side of both CMOD-4 and CMOD-5 sections. This is a clear sign that the GMF sections are too big at low winds (the cone section in this Figure corresponds to winds around 4.3 m/s). Moreover, the distribution of the simulated triplets (in plots b to f, the points are distributed at either sides of CMOD-5 sections), which are derived using CMOD-5, further confirms the GMF misfit at low winds. It is also discernible from Figure 3.1a that, although CMOD-5 shows some misfit, the latter better fits the real data than CMOD-4.

Taking into account the effect of using an imperfect GMF in the simulation (i.e., section expansion of triplet distribution), plot d is the simulated plot that resembles best the real data (plot a). The rest of the plots contain either too little (plots b and c) or too much (plots e and f) noise. Plot d corresponds to a wind variability of 0.5 m/s and 8 σ° samples. Therefore, from now on, we will use these parameters for further simulations.

Figure 3.2 shows more comparisons between the real and simulated (with the above determined parameters) triplets for the same cone section as Figure 3.1 but for node or wind vector cell (WVC) numbers 7 (top plots), 13 (mid plots) and 17 (bottom plots). Again, the mentioned GMF misfit at low winds is present in these plots (see difference in distributions between left and right plots). Looking at the excess of noise at the top of the simulated triplet distributions, one could conclude that the upwind/downwind region of CMOD-5 is too high. However, more research is required in order to consistently correct the mentioned misfit at the associated wind speed and incidence angle.

Again, taking into account the impact of such misfit in our plots, there is a good agreement between real and simulated triplets. As such, we can conclude that the selected geophysical noise

[1] Such value corresponds to the mean of the estimated instrument noise values in the ESA product, corrected in 2004.

parameters are realistic. Moreover, at higher wind speed (i.e., 6 m/s and above) cone sections, where the CMOD-5 GMF shows little misfit (except for the innermost WVCs), there is a very good agreement between the real and simulated data (not shown). However, here the relative contribution of the geophysical noise to the total noise is smaller (i.e., the instrument noise dominates the total *Kp* in Eq. 3.4), as expected from our parameter selection. At lower speeds, there is reasonable agreement. However, since the scattering of the triplets is of comparable size to the diameter of the cone section, the analysis is more difficult. Some inconsistency between real and simulated triplets appears (not shown) for the innermost WVCs (i.e., WVC numbers 1 to 3), where the instrument noise seems larger than specified for all wind speeds. At such WVCs, the backscatter sensitivity to incidence angle is maximal. In the simulation, we assume no footprint (sample) incidence angle variation within the same WVC. We have tested the effect of a realistic incidence angle variation among samples and indeed, the resulting simulated triplets now better agree with the real triplets at the innermost WVCs. However, there are still some outliers in the real triplet distributions, at the bottom part of the sections (crosswind), which remain unexplained (not shown). A more detailed investigation on the geophysical effects (maybe associated to certain geographical regions) that generate such excess of noise is required in order to improve the geophysical noise model.

.

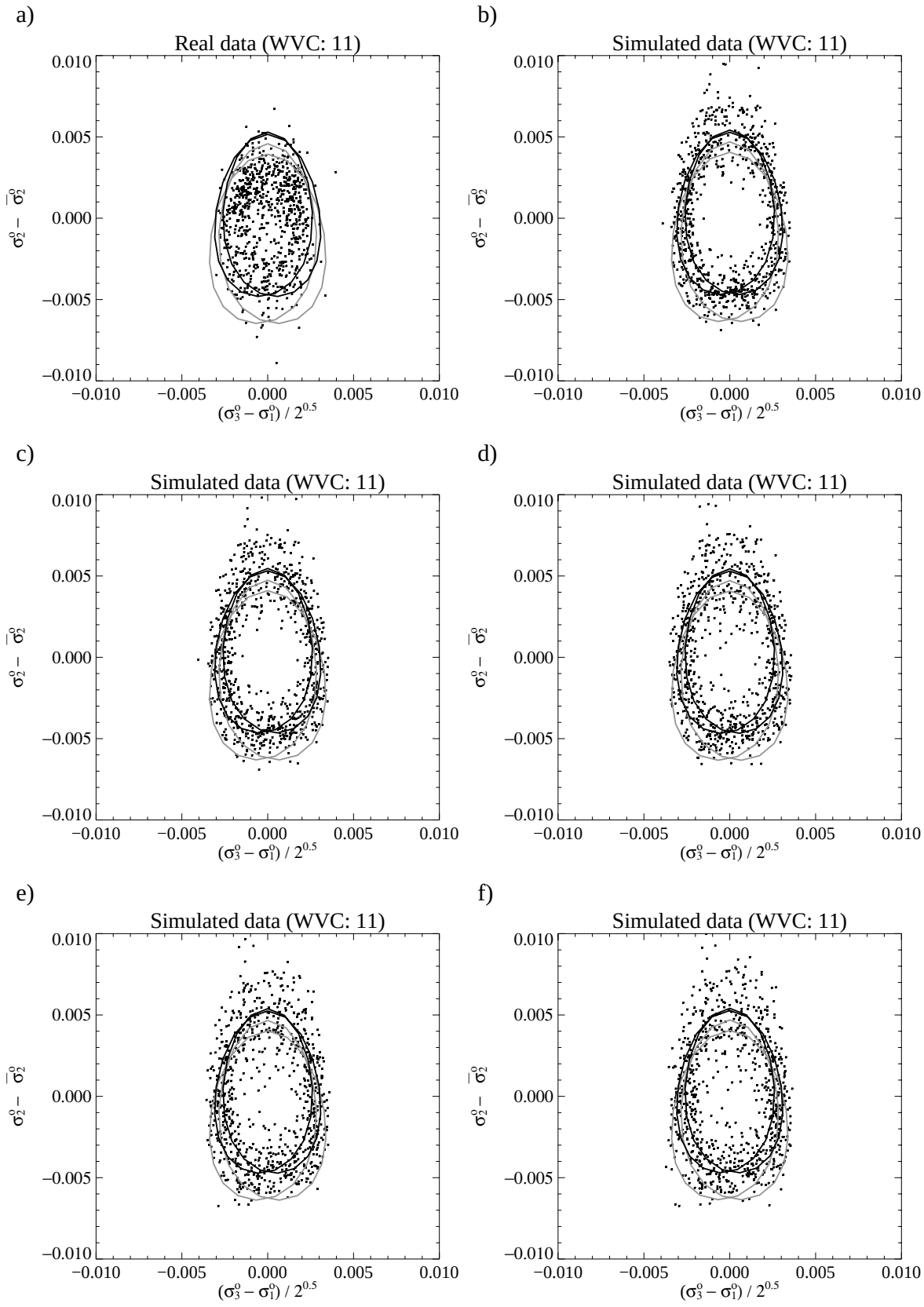

Figure 3.1 Intersection of the cone with the plane $\sigma^o_1 + \sigma^o_3 = 2\sigma^o_{ref}$, with a thickness of $0.05\sigma^o_{ref}$ for WVC 11, for values of σ^o_{ref} corresponding approximately to a speed of 4.3 m/s. Plot a shows the real triplet distribution; the rest of the plots correspond to simulated data assuming 8 σ^o samples and different wind variability values: 0.4 m/s (plot b), 0.45 m/s (plot c), 0.5 m/s (plot d), 0.55 m/s (plot e), and 0.6 m/s (plot f), respectively. The curves for both CMOD-4 (grey) and CMOD-5 (black) are plotted. The data have been offset by the mean of σ^o_2.

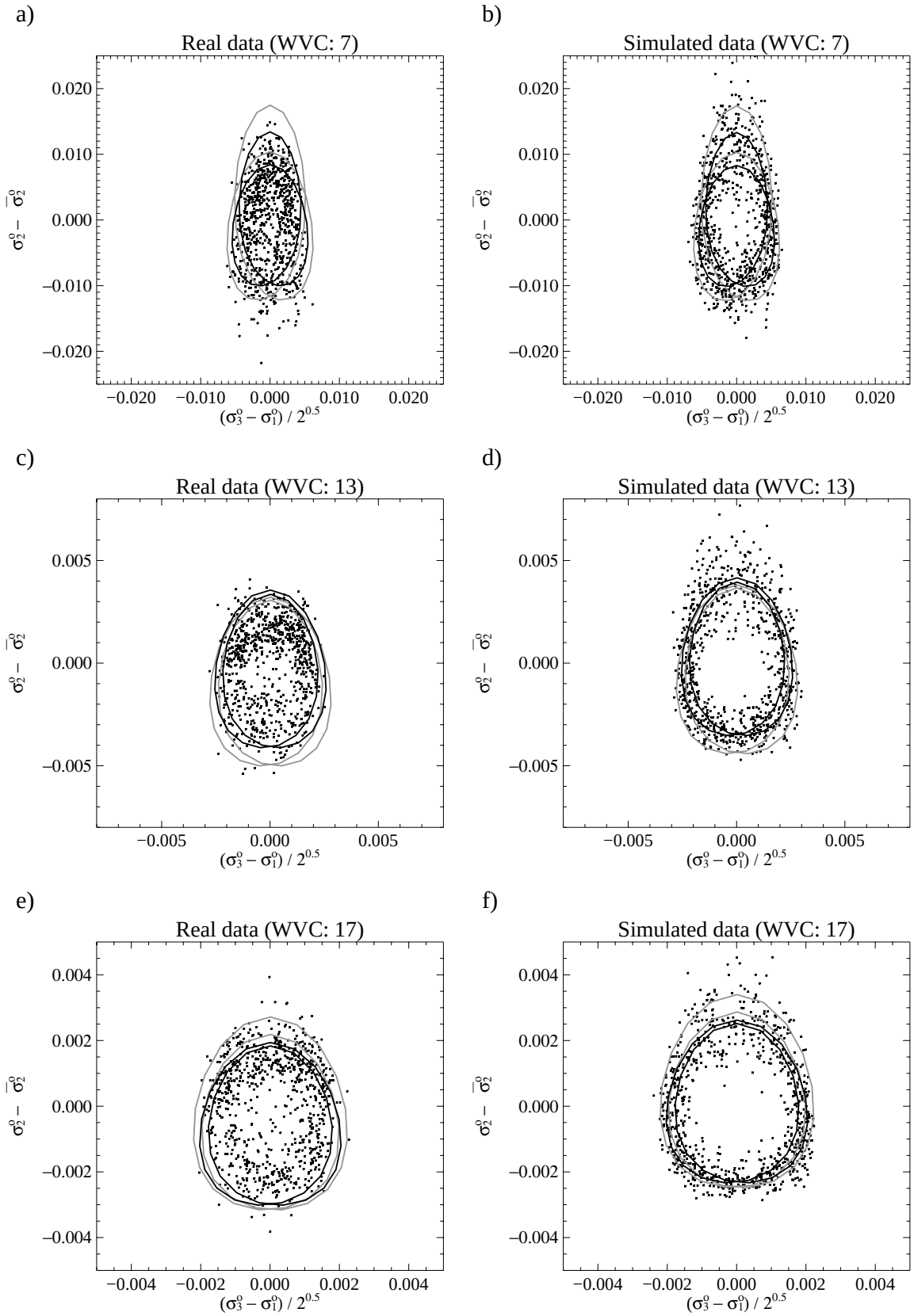

Figure 3.2 Same cone section as for Figure 3.1 but for WVC numbers 7 (top), 13 (mid), and 17 (bottom). The left plots show the real triplet distribution and the right plots show simulated triplets for a wind variability of 0.5 m/s and 8 σ^o samples.

3.1.2 Derivation of a geophysical noise model

In order to derive a geophysical noise model, we study the impact of the derived geophysical noise parameters (see section 3.1.1) on the mean σ^o value and its uncertainty (SD) in terms of dependencies on wind speed, wind direction, and incidence angle. This sensitivity study is performed over a wide range of wind speeds [0-20 m/s], wind directions [0°-360°], and incidence angles [16°-66°]. Thus, for any given "true" σ^o (corresponding to an input or "true" wind speed, wind direction and incidence angle within the mentioned ranges), a distribution of σ^o corresponding to a wind (component) variability of 0.5 m/s over the "true" wind is generated. The SD of the distribution is computed and reduced by a factor of $1/\sqrt{8}$ due to the noise level reduction in the averaging process (i.e., as determined in section 3.1.1, a total of 8 sub-cell σ^o samples are averaged for every ERS beam).

Figure 3.3 shows the difference between the mean of the σ^o distribution and the "true" σ^o as a function of wind direction and incidence angle, and for different wind speed values (solid line). It is clear that for high incidence angles and low winds (see plot b), the wind direction sensitivities play an important role, showing some significant biases at certain directions.

Another interesting exercise is to look at the σ^o corresponding to the "true" mean wind speed. For any wind distribution, the wind speed of the mean wind in wind components ("true" wind) is different from the mean of the wind speed ("true" mean wind speed), especially at low winds. Scatterometers actually observe the latter. The dotted lines in Figure 3.3 represent the σ^o difference between the "true" mean wind speed and the "true" wind. In order to better analyse the actual bias of the mean σ^o distribution we therefore have to look at the differences between the solid and the dotted lines. As it is discernible, the biases become smaller now.

However, these biases are corrected in the GMF by definition. That is, the GMF is a fit of the mean of the σ^o distribution to some reference ("true") winds. As such, the deviations of the mean σ^o from the "true" σ^o are taken into account in the GMF fit. Therefore, these biases are not expected to have any significant impact on the quality of wind retrieval. The uncertainty in the mean however would certainly have an effect.

The error bars in Figure 3.3 represent uncertainty in terms of geophysical noise. Dependencies on wind speed (see decreasing bar sizes from top to bottom plots), incidence angle (left plots) and wind direction (right plots) are clearly discernible. As such, the geophysical noise model should reflect these dependencies.

The inclusion of the wind direction dependency in the noise model could have a negative impact on wind retrieval however. As discussed in *Portabella and Stoffelen* (2001), the shape of the GMF surface makes certain wind directions to be favoured and therefore systematically assigned in the inversion. Including wind direction dependencies in the MLE (e.g., setting a wind direction dependent *Kp*) will most likely make such inversion problem more acute. As such, we compute a geophysical noise model dependent on wind speed and incidence angle only.

To neglect the wind direction dependency, we average the geophysical noise over all wind directions (error bar average of Figure 3.3 right plots). Figure 3.4a shows the average geophysical noise surface (Kp_{geoph}) as a function of wind speed and incidence angle. Since the estimated Kp_{instr} is available from the ESA product, the total *Kp* can be easily derived using equation 3.4.

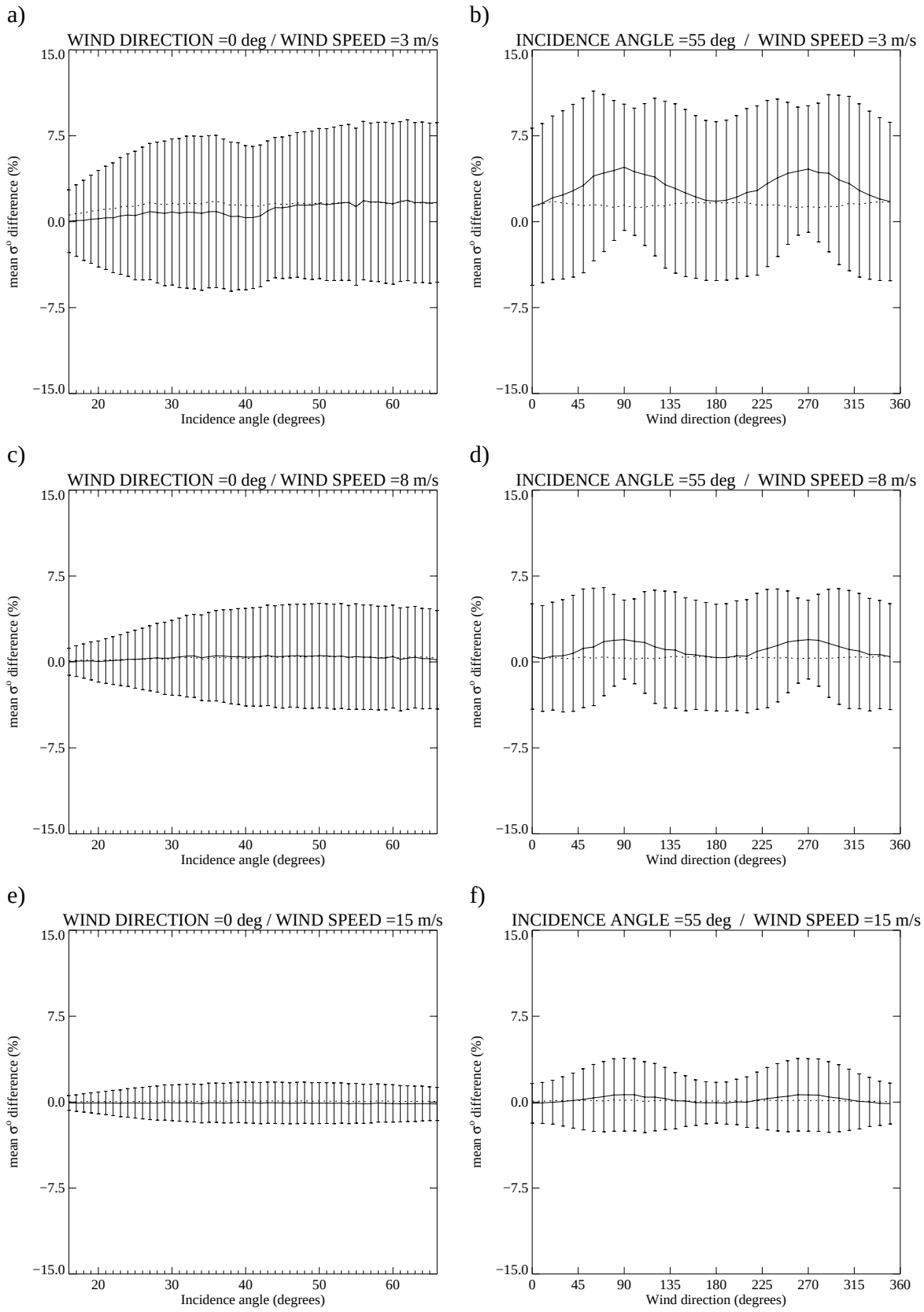

Figure 3.3 Difference as a function of incidence angles (left plots) and wind direction (right plots) between the mean of the sub-cell resolution σ^o's and the "true" σ^o (corresponding to the true mean wind) (solid); and between the σ^o corresponding to the true wind speed and the mentioned "true" σ^o(dotted). The bars represent the SD (in %) of the mean of the sub-cell resolution σ^o. The left plots correspond to a fixed wind direction of 0° and the right plots to a fixed incidence angle of 55°. The plots correspond to fixed speed values of 3m/s (top), 8m/s (mid) and 15m/s (bottom).

a)

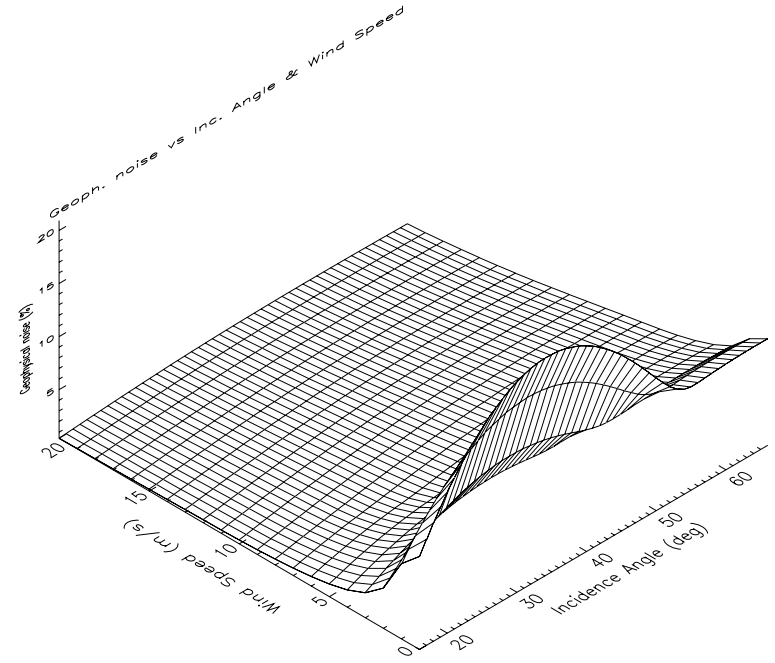

b)

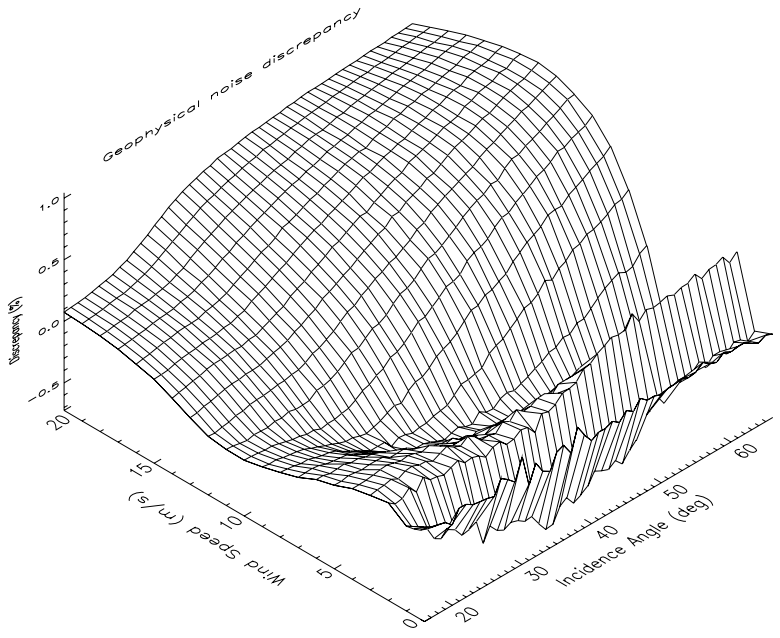

Figure 3.4 Average geophysical noise (plot a) and discrepancy between the average and the 0° geophysical noise (plot b) as a function of wind speed and incidence angle. The speed binning is 1 m/s and the angle binning is 1°.

In order to show the error in the estimation of Kp_{geoph} produced by neglecting the wind direction dependency, we show in Figure 3.4b the discrepancies between the average geophysical noise and the geophysical noise corresponding to a wind direction of 0°. The discrepancy is maximal at high incidence angles for high and very low wind speeds. However, taking into account that the estimated Kp_{instr} ranges from 3% to 5%, the impact of such discrepancies (up to 1%) in the total *Kp* is small. For latest developments on the ERS geophysical noise model, see Portabella and Stoffelen (2005).

3.1.3 Impact of *Kp* in wind retrieval

As discussed at the beginning of chapter 3, in order to retrieve accurate winds for ERS using the MLE inversion, it is important to make practicable the assumption of constant $p(\sigma_s^o)$. *Stoffelen and Anderson* (1997a) investigated the effect of normalization in equation 3.3 through visualization of differently scaled 3D measurement spaces, e.g., cone sections of Figures 3.1 and 3.2 have a scaling factor of 1. They show that to be able to obtain both accurate wind directions and a realistic wind direction probability density after inversion, it is desirable that equal portions of the σ^o triplets are thrown onto equal wind direction intervals. This is the case if the GMF surface has no sharp curvature and is circular rather than elliptic. (Note: A circular shape of the cone for a uniform wind direction probability density is equivalent to $p(\sigma_s^o)$ constant).

As it is discernible in Figure 3.2, the cone sections are rather elliptic, especially in the inner WVCs (see top plots). *Stoffelen and Anderson* (1997a) show that by using a fixed scaling (which is equivalent to no MLE normalisation) as in Figure 3.2 and by transforming the σ^o space to a z space, where $z = (\sigma^o)^{0.625}$, all the cone sections become circular.

Figure 3.5 shows the same cone sections as in Figure 3.2 but in a measurement space scaled by the derived *Kp* (see section 3.1.2). Both the real (left plots) and the simulated (right plots) triplet distributions show clear elliptic shapes rather than circular. These elliptic cone shapes are similar to the ones found by *Stoffelen and Anderson* (1997a) when scaling the measurement space by a constant 5% instrument *Kp*. The latter results in less accurate wind retrieval compared to the retrieval in z space.

Therefore, despite the use of a good measurement noise model in the MLE normalisation, the wind retrieval accuracy is not satisfactory since $p(\sigma_s^o)$ is far from being locally constant. In other words, the shape of the cone is more important than the noise properties of the system for wind retrieval.

According to these results, a space transformation, which makes true the assumption of constant $p(\sigma_s^o)$, i.e., z space, is desirable for ERS. Since one of the goals of this project is to set a generic method for scatterometer wind retrieval, we should now try to determine the corresponding space transformation for NSCAT or QuikSCAT. However, this is not straightforward. In contrast with ERS, where the transformation could be analytically derived since the measurement space is 3-dimensional, NSCAT and QuikSCAT measurement systems are 4-dimensional.

We therefore propose to set a generic method that seeks for the best measurement space transformation in a numerical way. Since the transformation is already performed for ERS, we

can use the latter to validate the proposed method (see chapter 4) and later apply it to SeaWinds (see chapter 5).

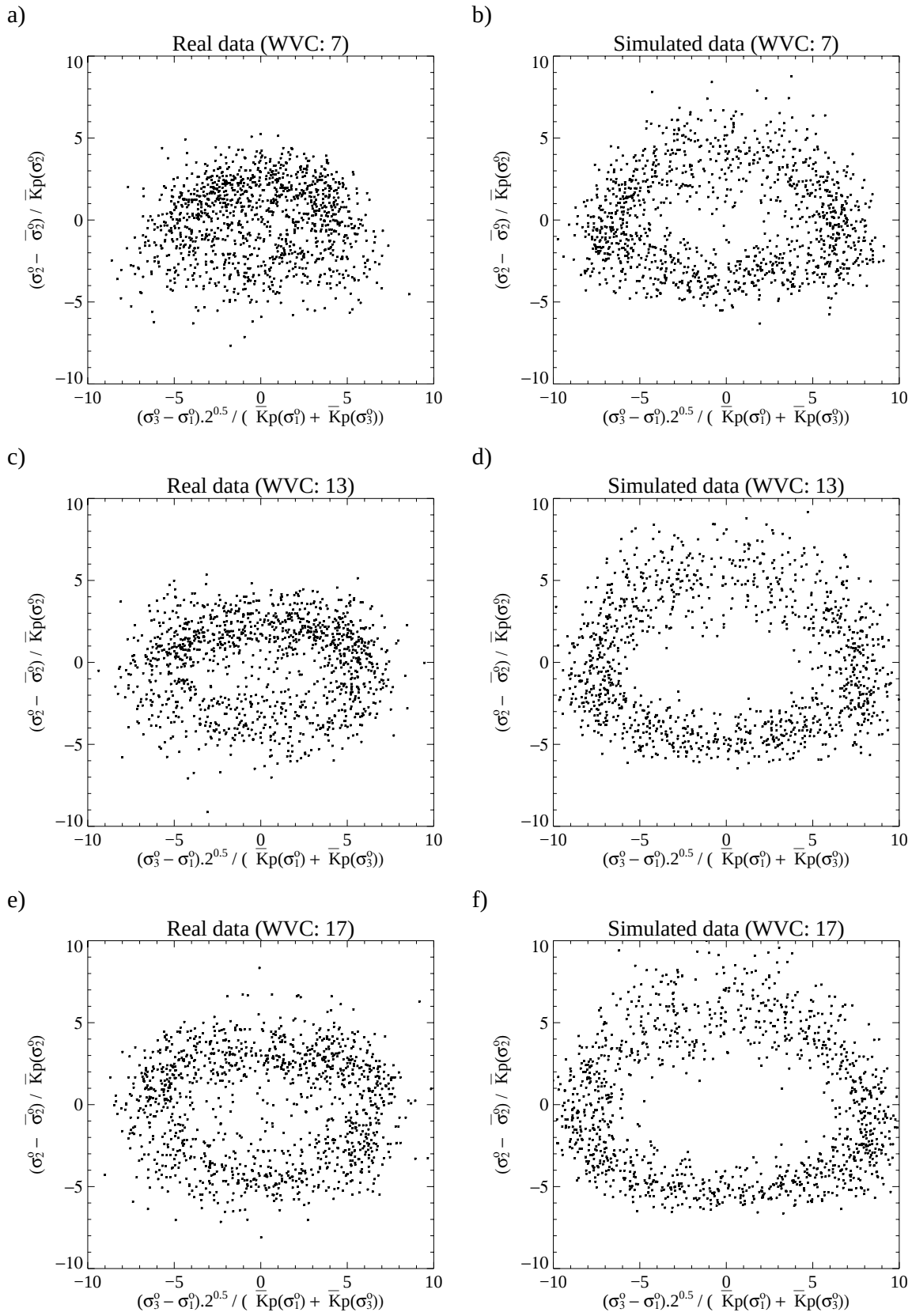

Figure 3.5 Same as Figure 3.2 but for triplet values scaled by Kp.

4 Wind Retrieval

4.1 ERS case

As discussed in the previous chapter, in order to be able to obtain both accurate wind directions and a realistic wind direction probability density after inversion, it is desirable that equal portions of the σ° triplets are thrown onto equal wind direction intervals, i.e., a constant $p(\sigma_s)$. This is the case if the GMF surface has no sharp curvature and is circular rather than elliptic. For ERS, the circularity of the cone is achieved by an analytically derived space transformation. An alternative method, which is generic for all scatterometers, based on the scaling or calibration of the different scatterometer beams is presented and validated for ERS in this chapter.

4.1.1 Calibration method

In order to look for an interesting property of circularity, which can be generically used by all scatterometers, let's first look at the 2-dimensional case.

A circle is defined by a set of two functions, which depend on an angle ϕ in the following way:

$$x = r \cdot \cos\phi \,;\; y = r \cdot \sin\phi \tag{4.1}$$

where x and y represent the horizontal and vertical axis, respectively, and r is the radius of the circle and therefore a constant value. From equation 4.1, it can be easily derived the following expression of the total sensitivity:

$$\left\| \frac{\partial \vec{x}}{\partial \phi} \right\| = \left(\frac{\partial x}{\partial \phi} \right)^2 + \left(\frac{\partial y}{\partial \phi} \right)^2 = \text{constant} \tag{4.2}$$

That is, the total sensitivity to direction changes remains constant for any value of ϕ, ranging from 0° to 360°. Or, in other words, the distance $\vec{x}$ travelled for a small change in ϕ is the same for all ϕ.

Similarly, such constant-distance property can be applied in scatterometry to any N-dimensional measurement system. As such, constant-distance is true when a set of functions, i.e., σ° beams, which depend on an angle ϕ, i.e., wind direction, follow the expression:

$$\left\| \frac{\partial \overrightarrow{\sigma^o}}{\partial \phi} \right\| = \sum_{i=1}^{N} \left(\frac{\partial \sigma_i^o}{\partial \phi} \right)^2 = \text{constant} \tag{4.3}$$

where N=3 for ERS, and N=4 for NSCAT or SeaWinds. Therefore, in order to obtain circularity, we must make equation 4.3 as true (i.e., constant) as possible. That is, when equation 4.3 is not true, we must find a transformation of $\overrightarrow{\sigma^o}$, i.e., $\overrightarrow{\sigma'}$, which satisfies the following:

$$\left\| \frac{\partial \overrightarrow{\sigma'}}{\partial \phi} \right\| \approx \text{constant} \tag{4.4}$$

Minimization

The left plots of Figure 4.1 represent the total sensitivity (solid curves) of CMOD-5 GMF as a function of wind direction for a few WVC numbers and wind speed values. The dotted, dashed, and dash-dotted curves represent the individual fore-, mid- and aft-beam sensitivities, respectively, which contribute to the total sensitivity (see equation 4.3). The straight line corresponds to the mean total sensitivity over all wind directions:

$$Mean = \frac{1}{M} \sum_{j=1}^{M} \sum_{i=1}^{3} \left(\left. \frac{\partial \sigma_i^o}{\partial \phi} \right|_{\phi_j} \right)^2 \tag{4.5}$$

where M is the number of wind direction intervals, i.e., 360 in this case.

As it is discernible from these plots, using Kp normalization in the MLE inversion (see equation 3.3) makes the cone far from being circular (note that the solid curves are far from being straight lines).

The goal of the method that we propose is to flatten as much as possible the mentioned (solid) curves. In order to do so, we scale the individual beam sensitivities such that the resulting total sensitivity is closest to its mean value. In other words, we minimize the distance between the solid curve (total sensitivity) and the straight line (mean value) by re-scaling the dotted, dashed and dash-dotted lines (individual beam sensitivities). As such, the cost function we want to minimize looks as follows:

$$J = \frac{1}{M} \sum_{j=1}^{M} \left[\sum_{i=1}^{3} \left(a_i \cdot \left. \frac{\partial \sigma_i^o}{\partial \phi} \right|_{\phi_j} \right)^2 - Mean \right]^2 \tag{4.6}$$

where J is the cost function and a_i the scaling or calibration coefficients. Note that since $a_i \neq a_i(\phi)$, the minimization is analogous to looking for a transformation (scaling) $\overrightarrow{\sigma'} = \vec{a} \cdot \overrightarrow{\sigma^o}$, which obeys equation 4.4.

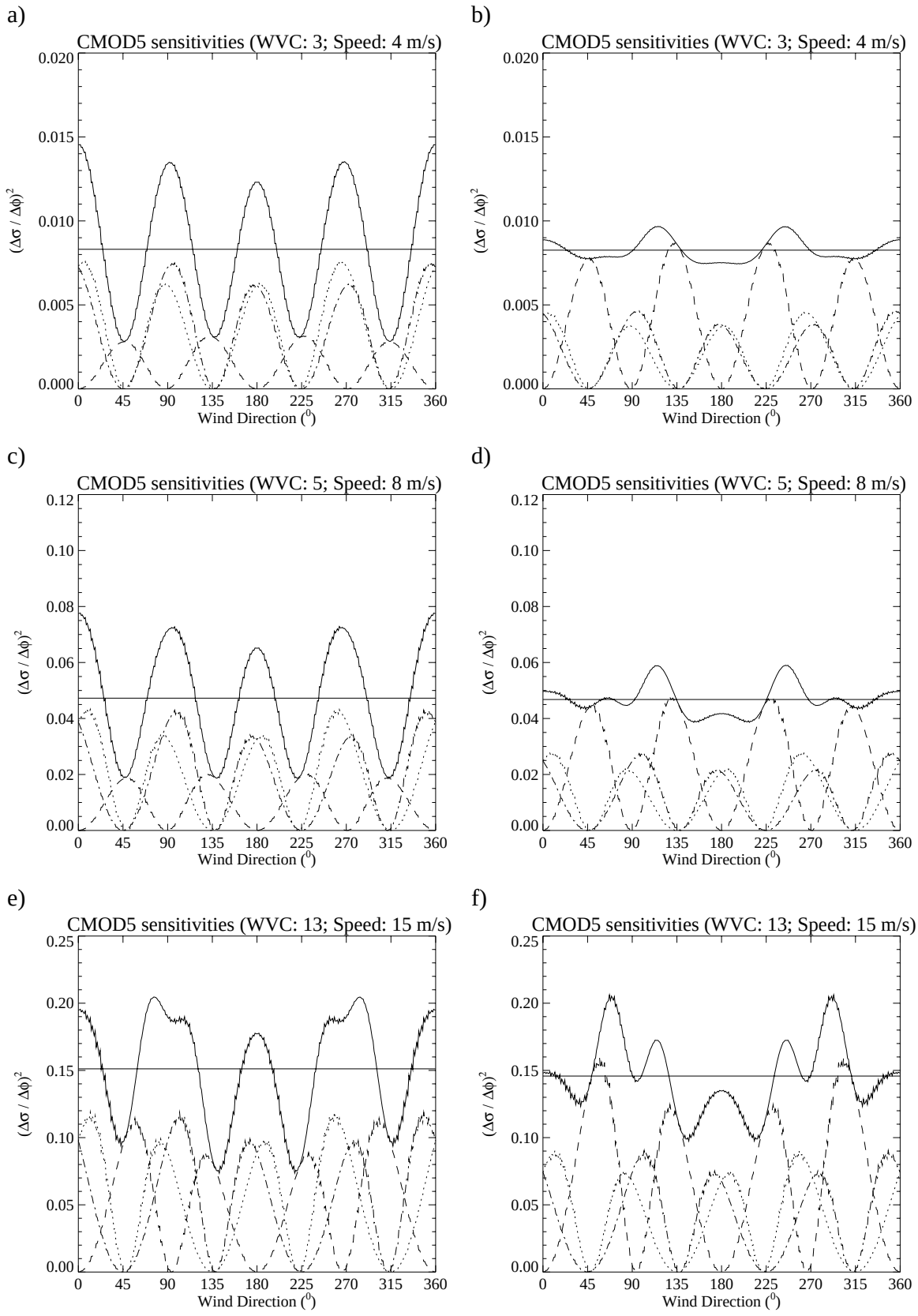

Figure 4.1 CMOD-5 total sensitivity (solid curves) as a function of wind direction for Kp norm (left plots) and calibrated Kp norm (right plots) for a few WVC numbers and wind speed values: WVC 3 and 4 m/s (top plots), WVC 5 and 8 m/s (mid plots), and WVC 13 and 15 m/s (bottom plots). The dotted, dashed, and dash-dotted curves represent the individual fore-, mid- and aft-beam sensitivities, respectively. The straight line corresponds to the mean total sensitivity over all wind directions.

Also note that we have chosen the squared distance (between total sensitivity and the mean) rather than the distance (see equation 4.6) for minimization since the results (not shown) reveal that the former is more effective than the latter in flattening the total sensitivity curve.

For every wind speed and WVC number, J is minimized and a set of a_i found. The minimization results in a clear single minimum (for every wind speed and WVC number), indicating that the method is robust and un-ambiguous. For more detailed information on the a_i coefficients, see appendix A.

The left plots from Figure 4.1 show the sensitivity in σ^o space (from here on referred to as "Kp norm", since it uses Kp normalization in the MLE inversion) and the right plots show the sensitivity in σ' space, i.e., after calibration (from here on referred to as "calibrated Kp norm"). By comparing either sides of Figure 4.1, one can easily see that, in general, the calibration is effective in flattening the total sensitivity curve, i.e. making the cone more circular. The calibration is most effective for low and mid winds at the inner swath (WVC numbers 1-6) region (see top and mid plots). However, it is little effective for high winds and the outer swath (WVC numbers 13-19) region (see bottom plots). In this case, the individual beam sensitivities (see Figure 4.1e) contribute in a similar way to the total sensitivity (in contrast with Figures 4.1a and 4.1c, where fore and aft beams especially contribute to the peaks while the mid beam contributes to the troughs), and therefore scaling does not help much in flattening the total sensitivity curve.

Another interesting result is that the mean total sensitivity remains almost the same after calibration (compare straight lines at either sides of Figure 4.1), denoting consistency in the calibration procedure. More results on the calibration skill are shown in Figures 4.2 and 4.3.

Figure 4.2 shows the histograms of the gradient[1] of the total sensitivity curves from Figure 4.1. The dotted lines correspond to histograms of Kp norm and the solid lines to histograms calibrated Kp norm. The distribution of gradients shows how flat the total sensitivity curve is, i.e., the lower the gradients are, the flatter the total sensitivity curve. Figures 4.2a and 4.2b show a much

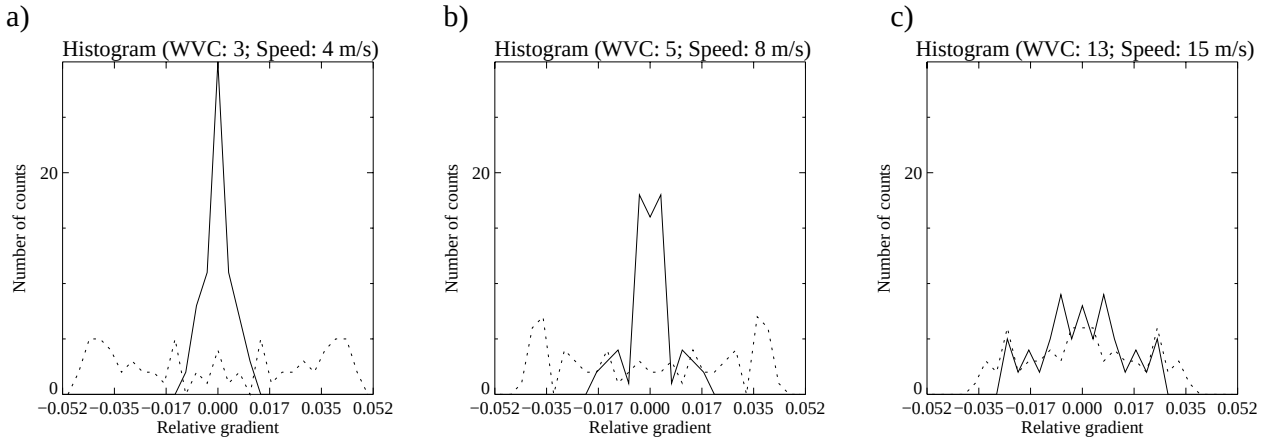

Figure 4.2 Histograms of the gradients of the total sensitivity curves from Figure 4.1 for a few WVC numbers and wind speed values: (a) WVC 3 and 4 m/s, (b) WVC 5 and 8 m/s, and (c) WVC 13 and 15 m/s. The gradient values are relative to the mean total sensitivity. The dotted lines correspond to histograms of Kp norm and the solid lines to histograms of calibrated Kp norm.

[1] The noise of the total sensitivity curves in Figure 4.1 is filtered out by an averaging procedure to produce the results shown in Figures 4.2 and 4.3. This noise is a numerical artefact produced by the different wind direction sampling between the curves (1°) and the CMOD-5 look-up-table (2.5°) and, as such, has no geophysical meaning.

narrower gradient distribution around zero after calibration (see difference between solid and dotted distributions), denoting the good skill of the calibration procedure for low/mid wind speeds and inner swath region. Figure 4.2c shows almost no difference in the distributions before and after calibration, denoting the reduced effectiveness of the procedure for high winds and the outer swath.

Figure 4.3 shows the relative modulation (solid) and relative width of the minimum (dotted) of the total sensitivity curves from Figure 4.1 with respect to WVC number before (left) and after (right) calibration. The lower the modulation is, the flatter the sensitivity curve. Similarly, the larger the width of the minimum is, the flatter the sensitivity curve will most likely be. When comparing the left plots to the right plots, we see a drop in the modulation and an increase in the width of the minimum after calibration, denoting that, in general, the calibration is effective in flattening the total sensitivity curves.

Looking at the Kp norm results (left plots), we see that the sensitivity is flatter, i.e., more circular cone, as we increase the WVC number (see decrease of modulation and increase of minimum width with WVC number). This tendency is reversed after calibration (right plots), denoting a skill increase as the WVC number decreases. This is in line with the previously mentioned effectiveness of the procedure at the inner swath.

Looking at the right plots, it is also discernible that the calibration is more effective at low and mid winds than at high winds (compare Figure 4.3f with Figures 4.3b and 4.4d).

4.1.2 Validation

In this validation, we mainly show results in terms of wind direction skill since the calibration procedure is expected to improve this component most. Moreover, the results (not shown) reveal no significant wind speed skill difference between the three inversion types tested here, i.e., z space, Kp norm and calibrated Kp norm. The z-space inversion is used here as a reference since such transformation produces the most circular cone (see *Stoffelen and Anderson, 1997a*).

Figure 4.4a shows the two-dimensional histogram of the calibrated Kp norm wind direction solution closest to Kp norm 1st rank solution versus the latter. It is discernible that the difference between both wind direction distributions is rather small, i.e., standard deviation (SD) of only 3.6°. However, if we compare these two inversion schemes (Kp norm and calibrated Kp norm) to the z space one (see Figures 4.4b and 4.4c), we clearly see that the calibrated Kp norm is closer to z space than the Kp norm. Moreover, the calibrated Kp norm is closer to z space than to Kp norm (compare SD scores from Figures 4.4a and 4.4c). These results consequently indicate that by calibration we succeed in making the cone more circular.

Verification with ECMWF

Table 4.1 shows the root mean square (RMS) of the zonal (u) and meridional (v) wind component difference between ECMWF and the three ERS inversion types tested here. The general results show marginal differences among the latter with respect to ECMWF. Therefore, we can conclude

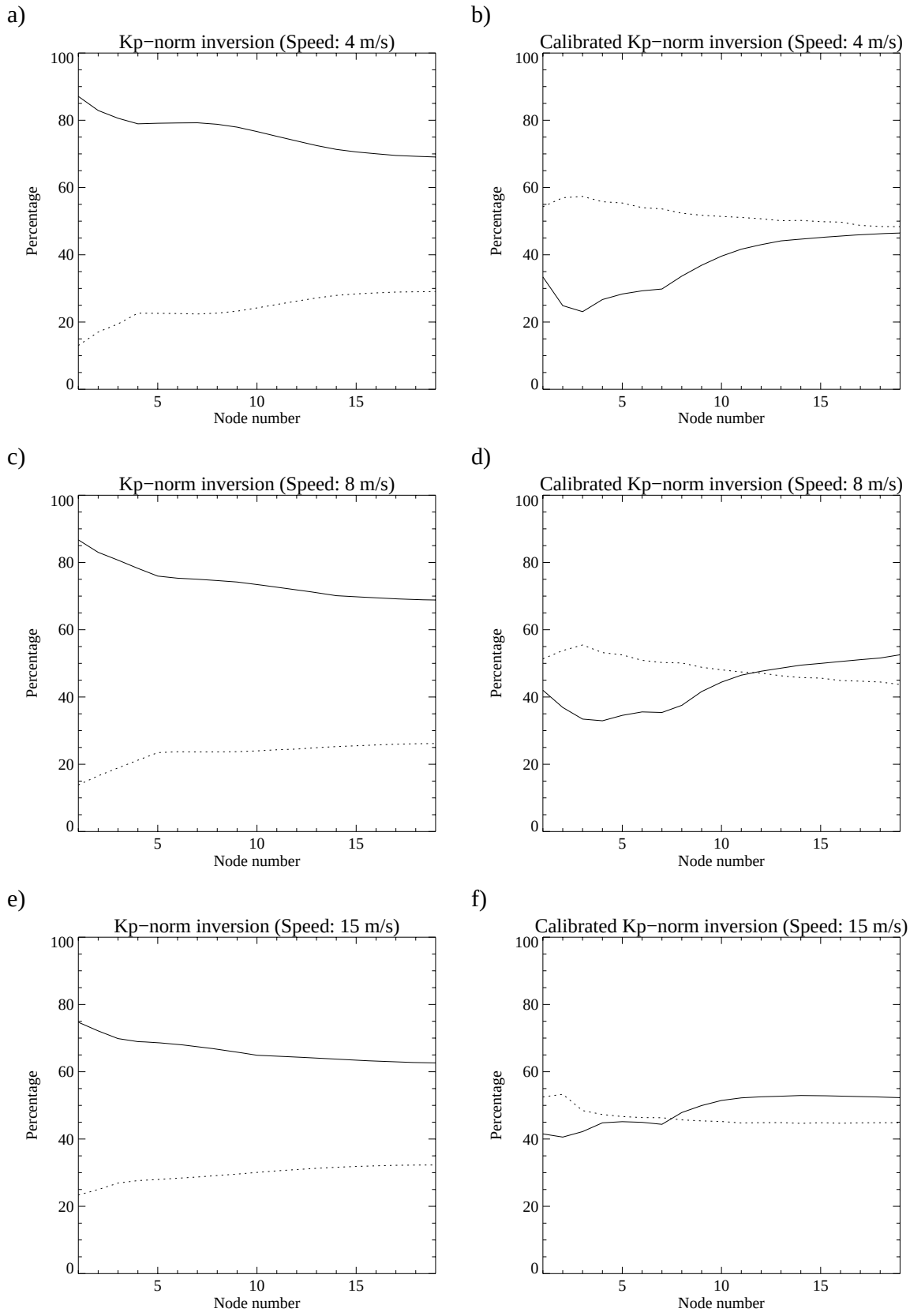

Figure 4.3 Relative modulation (difference between maximum and minimum relative to the origin) (solid) and relative width of the minimum (difference between the minimum value and the mean value over an interval of ±45° around the minimum) (dotted) of the total sensitivity curves from Figure 4.1 with respect to WVC number, for Kp norm (left) and calibrated Kp norm (right) and for different wind speed values: 4 m/s (top), 8 m/s (mid), and 15 m/s (bottom).

that in general, the quality of the different inversion schemes is comparable. However, a few differences arise when we look at the wind direction skill.

The schemes which approach a circular cone, i.e., z space and calibrated Kp norm, are expected to perform better than the Kp norm scheme where the latter shows less circularity (more ellipticity), i.e., in the inner swath (see section 4.1.1). Figure 4.5 shows the two-dimensional histograms of the ERS-retrieved wind solution closest to ECMWF versus ECMWF, for the three ERS inversion types. We note that the SD for z space is lower than for Kp norm (see Figures 4.5a and 4.5b), denoting a somewhat better wind direction skill for the former. After calibrating Kp norm, the wind direction skill is similar to the one for z space (see SD scores from Figures 4.5a and 4.5c).

Table 4.1 Mean RMS[1] (m/s).

	U component	V component
z space	2.05	2.18
Kp norm	2.07	2.18
Calibrated Kp norm	2.05	2.18

[1] The RMS is referred to as the RMS of the zonal (u) and meridional (v) wind component difference between ECMWF and the different ERS inversion types shown in the table.

The shape of the cone plays a crucial role in the wind direction retrieval. As the cone becomes more elliptic (less symmetric), certain directions are favoured in the retrieval process, causing in turn some artificial accumulations in the retrieved wind direction distributions. This systematic effect becomes more acute for points lying far away from the cone surface, i.e., for triplets with high MLE values.

Figure 4.6 shows the wind direction distributions for triplets with MLE larger than 0.7 (note that triplets with MLE larger than 9 are screened out). Looking at the left plots, some systematic accumulations at certain wind directions are discernible in the ERS-retrieved distributions (dotted) with respect to the ECMWF distributions (solid). These accumulations are largest for Kp norm inversion (Figure 4.6c) and smallest for z space (Figure 4.6a). The calibration (Figure 4.6e) reduces the problem with respect to the Kp norm inversion, although it is not as effective as the z-space transformation.

However, if we look at the inner swath distributions (right plots), the region in which the calibration is optimal (see section 4.1.1), it is clear that the calibrated Kp norm distribution (Figure 4.6f) is very similar to the z space one (Figure 4.6b), and much improved with respect to the Kp norm distribution (compare peaks at 0° and 180° in Figures 4.6d and 4.6f). Note that although these triplets have high MLE values, they are still of reasonable quality (see reasonable agreement between ECMWF and ERS-retrieved distributions from top and bottom plots) and therefore very important to keep since they represent about 4% of the total amount of the ERS wind observations.

Finally, we have also looked at the ERS inversion problem for low winds (not shown). The results show no significant differences between the three inversion types, which show substantial

wind direction errors. The reason for this is that the backscatter noise for low winds is very high as compared to the size of the cone, leading to systematic errors in the wind direction assignment (accumulations in the wind direction distributions).

In summary, we conclude that although z space is the optimal transformation for ERS in terms of the wind direction retrieval, the proposed calibration method represents an improvement with respect to Kp norm and therefore an alternative to z space. In contrast to z space, the calibration method is generic and can be applied to any scatterometer system. As such, in the next chapter we apply this method to SeaWinds.

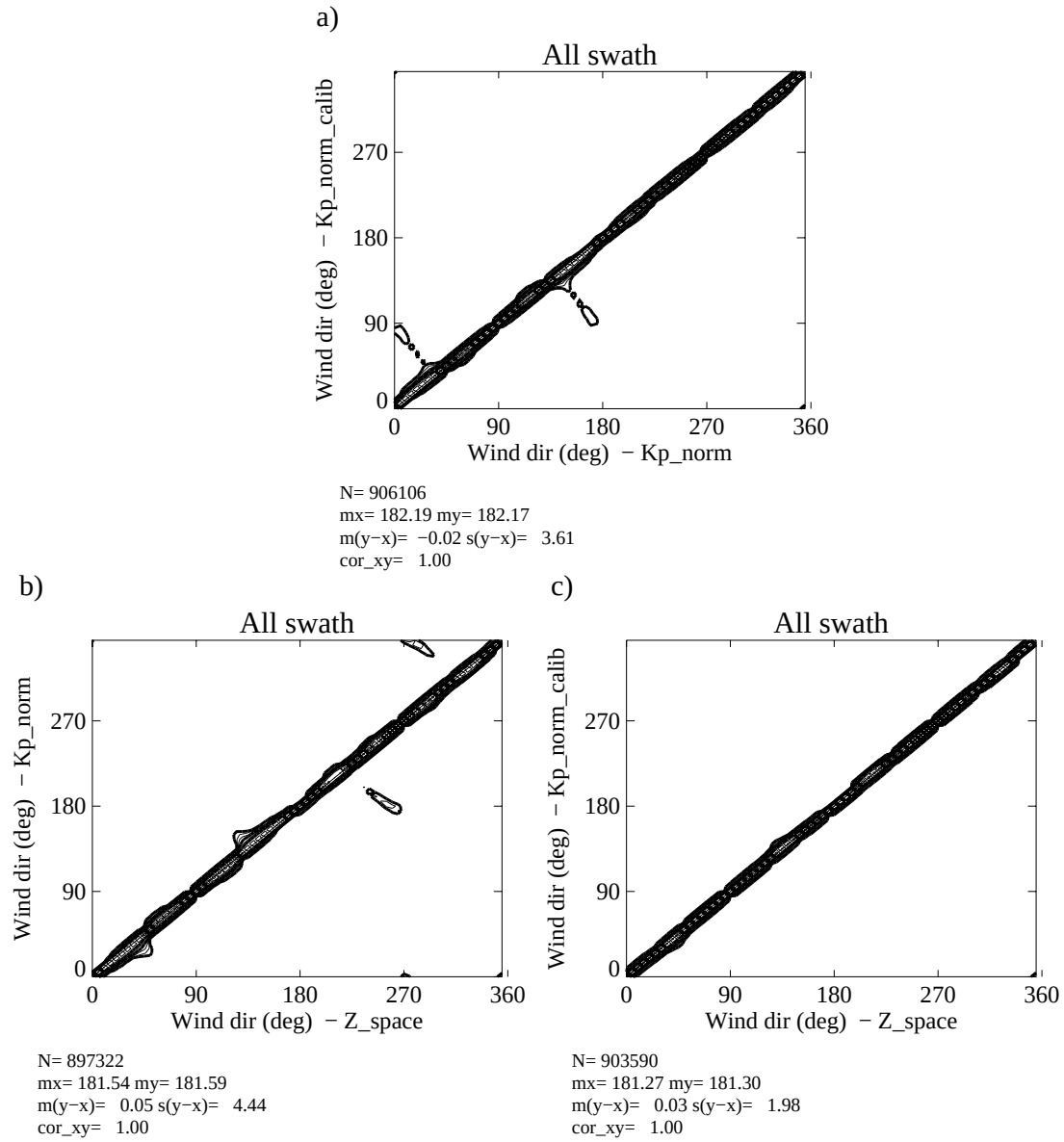

Figure 4.4 Two-dimensional histogram of the calibrated Kp norm wind direction solution closest to Kp norm 1st rank solution versus the latter (a), calibrated Kp norm direction solution closest to z space 1st rank solution versus the latter (b), and Kp norm direction solution closest to z space 1st rank solution versus the latter (c) in bins of 2.5 °. The histograms are computed for winds larger than 4 m/s. N is the number of data; mx and my are the mean values along the x and y axis, respectively; m(y-x) and s(y-x) are the bias and the standard deviation with respect to the diagonal, respectively; and cor_xy is the correlation value between the x- and y-axis distributions. The contour lines are in logarithmic scale: each step is a factor of 2 and the lowest level (outer-most contour line) is at N/16000 data points.

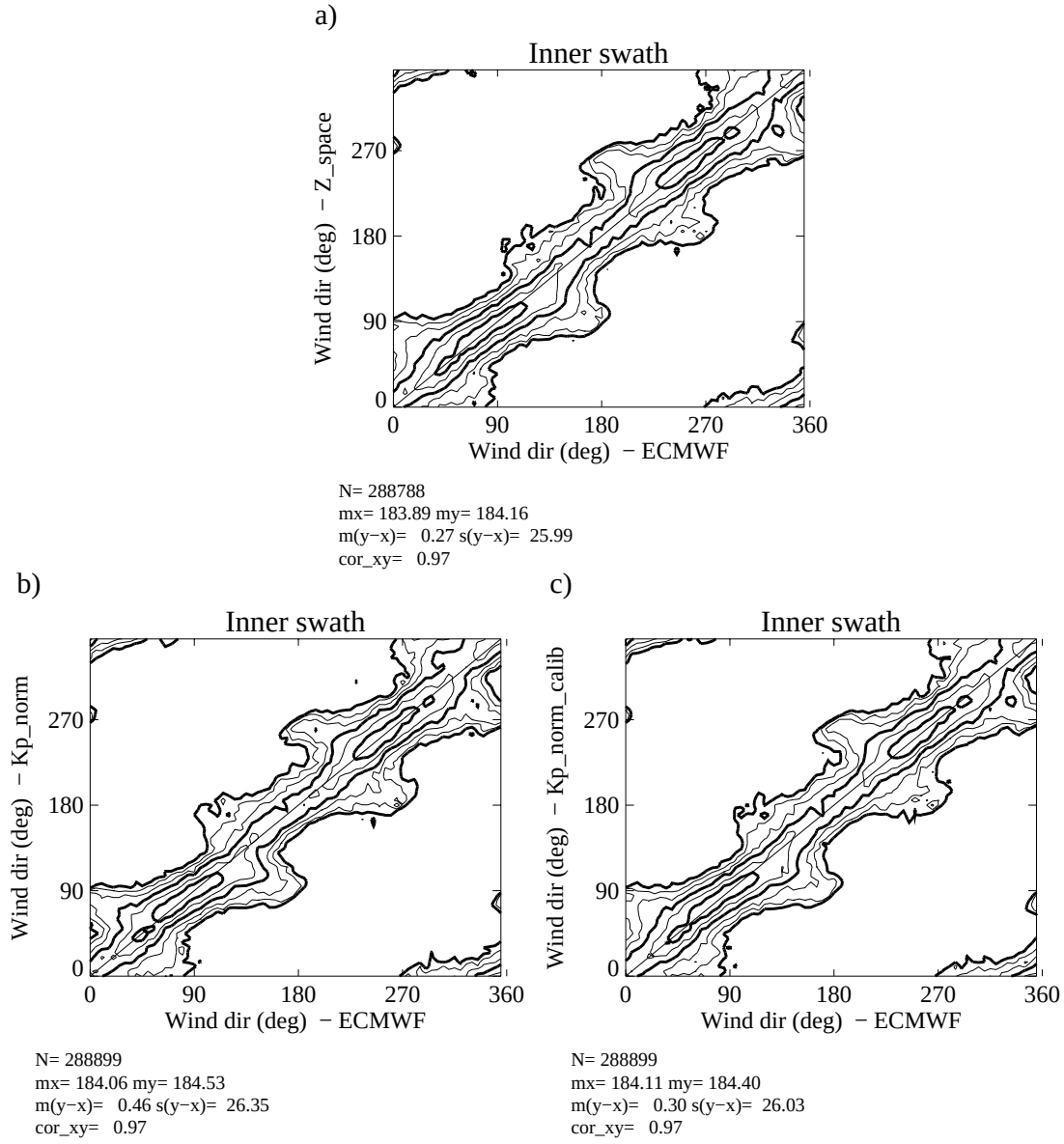

Figure 4.5 Two-dimensional histogram of the z space (a), Kp norm (b), and calibrated Kp norm (c) wind solution closest to ECMWF wind versus ECMWF in bins of 2.5°. Only data from the inner swath (WVC numbers 1-6) are plotted. The legend and contour lines are the same as in Figure 4.4.

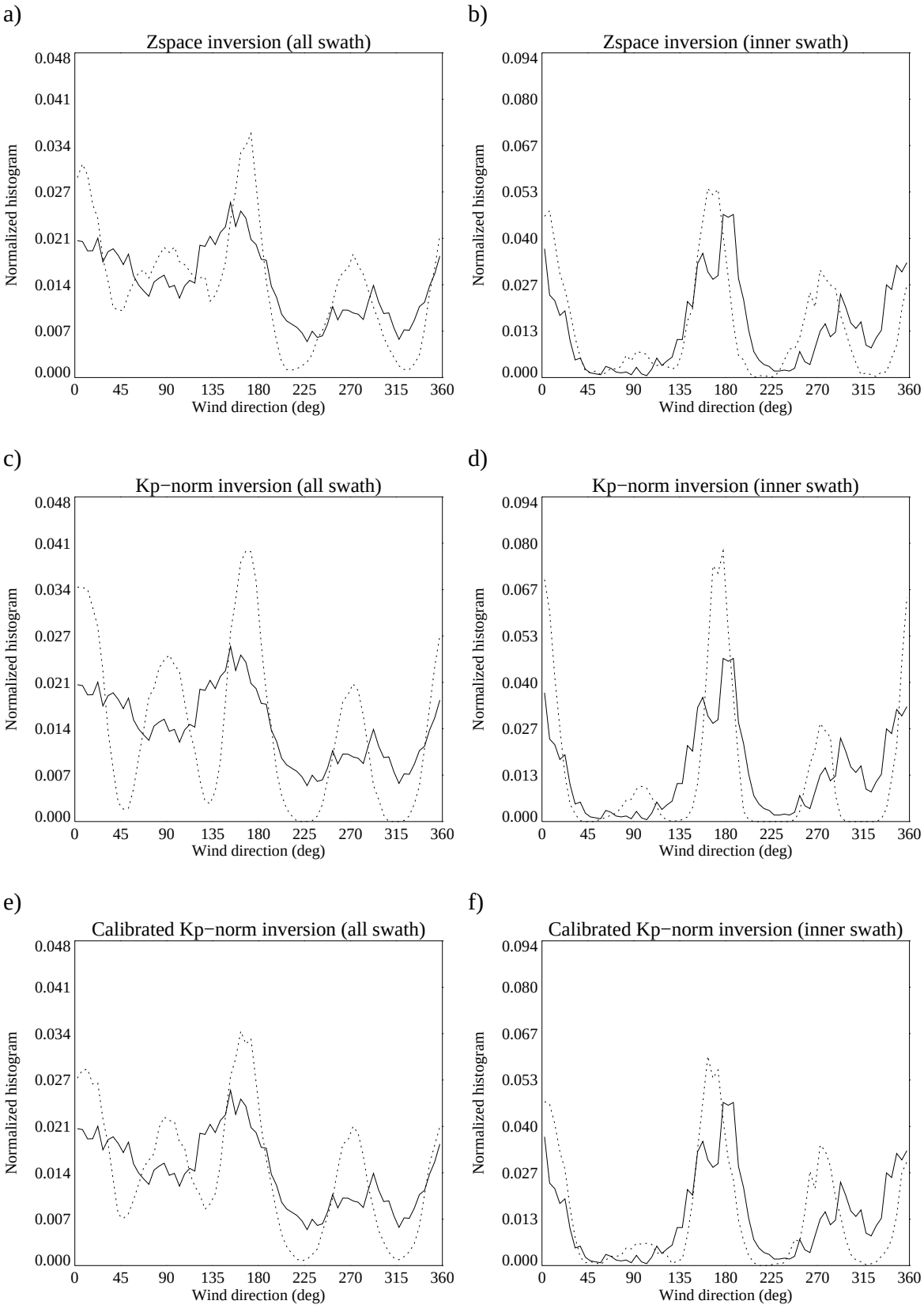

Figure 4.6 Wind direction (with respect to the satellite flight direction) distribution of the ERS-retrieved solution closest to ECMWF (dotted) for z space (top), Kp norm (mid), and calibrated Kp norm (bottom) and for the inner swath (right) and the entire swath (left). The solid line corresponds to the ECMWF wind direction distribution. The distributions only contain triplets with MLE larger than 0.7. The direction binning is 5 °.

4.2 SeaWinds case

The generic calibration method presented in section 4.1.1 is tested here for SeaWinds. Discussions on the wind direction retrieval limitations for SeaWinds and ways to overcome such limitations are included in this chapter.

4.2.1 Calibration skill

An important conclusion from chapter 3, is that the shape of the solution surface is more important than the noise properties for inversion. As such, there is no additional motivation to derive the geophysical noise for SeaWinds inversion purposes and no Kp normalisation is used in the MLE inversion (see equation 3.3). Similar to ERS, equations 4.5 and 4.6 are used for SeaWinds calibration.

Figure 4.7 is similar to Figure 4.1 but for SeaWinds. It represents the total sensitivity (solid curves) of NSCAT-2 GMF (*Wentz and Smith, 1999*) as a function of wind direction for a few WVC numbers and wind speed values, before (left plots) and after (right plots) calibration. By comparing either sides of Figure 4.7, one can easily see that, in general, the calibration is little effective in flattening the total sensitivity curve, i.e., making the solution surface more circular.

Comparing the left plots of Figures 4.1 and 5.1, there are certain wind directions for SeaWinds (Figure 4.7) with almost null total sensitivity, whereas for ERS (Figure 4.1) the low sensitivity areas are far from being insensitive (i.e., far from zero). In general, this behaviour can be seen at any across swath position (WVC number) and any wind speed regime. It is mainly due to the relative geometry of the SeaWinds beams and to the behaviour of the wind direction sensitivity of the horizontally polarized (H-pol) beams.

By looking at the individual beam sensitivities (non-solid curves) that contribute to the total sensitivity (solid curve) in the left plots of Figure 4.7, one can easily understand the problem. On the one hand, the relative beam geometry of many WVCs (see, for example, Figures 5.1c and 5.1e) produces areas where the sensitivity is minimum (and nearly zero) for all four beams. On the other hand, when the relative geometry is optimal, i.e., the minimum sensitivities of all beams are not aligned but rather the opposite, the large upwind-downwind asymmetry of the H-pol beams results in vast wind direction regions with almost no (individual beam) sensitivity (see dotted and dashed-dotted curves in Figure 4.7a in the range [–90°, 90°]). The latter in turn produces very-low total sensitivity regions as well.

In Figure 4.7, the calibrated sensitivities (right plots) show almost no difference with respect to the non-calibrated sensitivities (left plots), denoting that the calibration was little effective. Given the “null” sensitivity areas discussed above, this is a result to anticipate. It is clear that there is no way to flatten the total sensitivity when there are areas of null sensitivity. In the cases where the relative geometry is optimal, up-weighting the H-pol sensitivity is useless because of the large

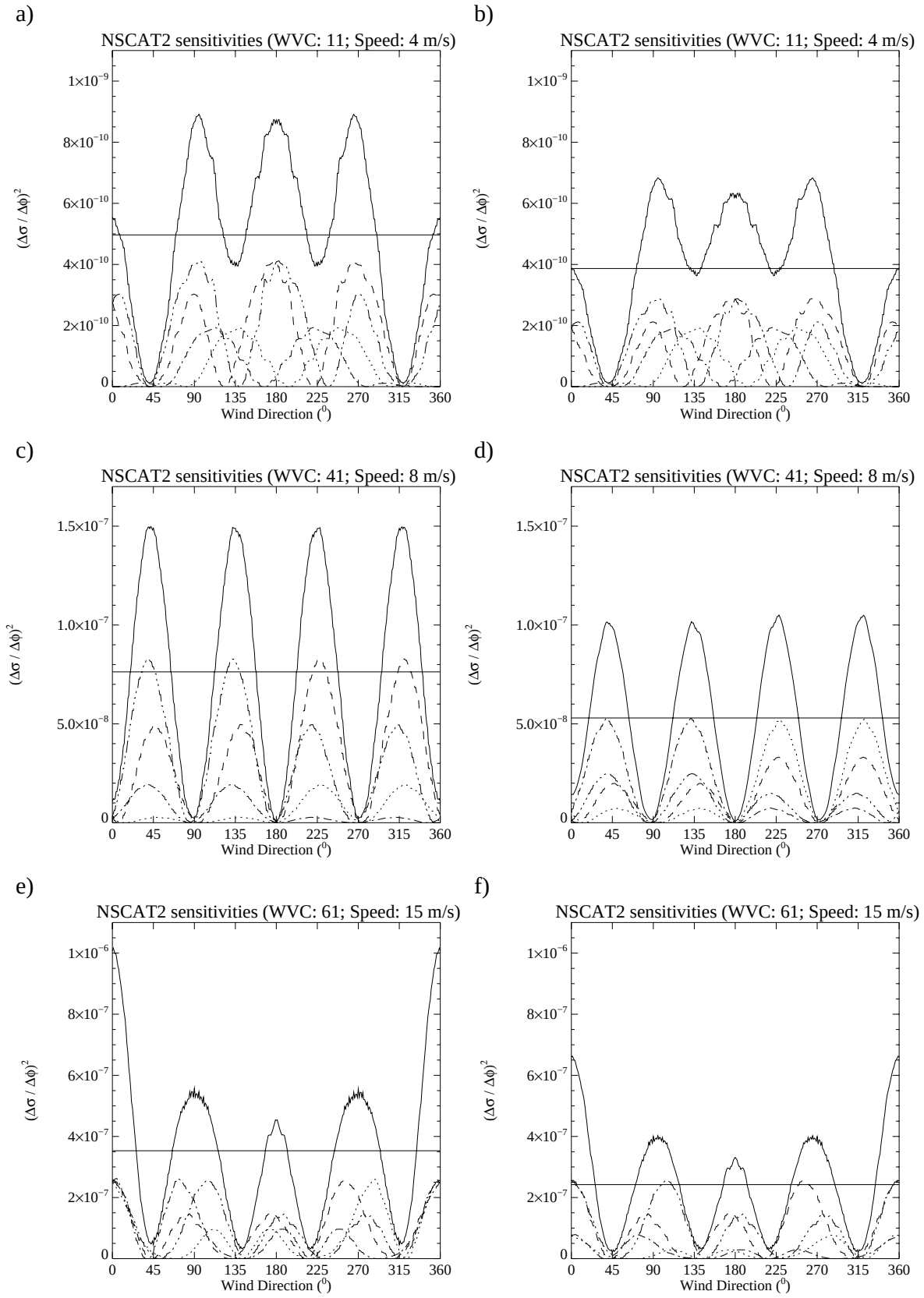

Figure 4.7 NSCAT-2 total sensitivity (solid curves) as a function of wind direction, before (left plots) and after (right plots) calibration, for a few WVC numbers and wind speed values: WVC 11 and 4 m/s (top plots), WVC 41 and 8 m/s (mid plots), and WVC 61 and 15 m/s (bottom plots). The dotted, dashed, dash-dotted, and dash-dot-dot-dotted curves represent the individual fore-inner, fore-outer, aft-inner, and aft-outer beam sensitivities, respectively. The straight line corresponds to the mean total sensitivity over all wind directions.

upwind-downwind asymmetry (in Figure 4.7a, a large weight in the dotted and dash-dotted lines will adequately increase the sensitivity around 45° and 315°, but in turn will excessively increase the sensitivity around 130° and 230°).

In contrast with ERS (see section 4.1.1), the mean total sensitivity substantially changes after calibration (compare straight lines at either sides of Figure 4.7), denoting a poor minimization of the cost function (see equation 4.6). The problem is that the cost function contains very broad minima. As such, the minimization procedure looks for drastic changes in the weighting (calibration coefficients) looking for better-defined minima. However, there are no defined minima, and instead, one of the many similar minima is selected in the end. An example for this is shown in Figure 4.8. The latter shows two different cuts of the cost function for SeaWinds.

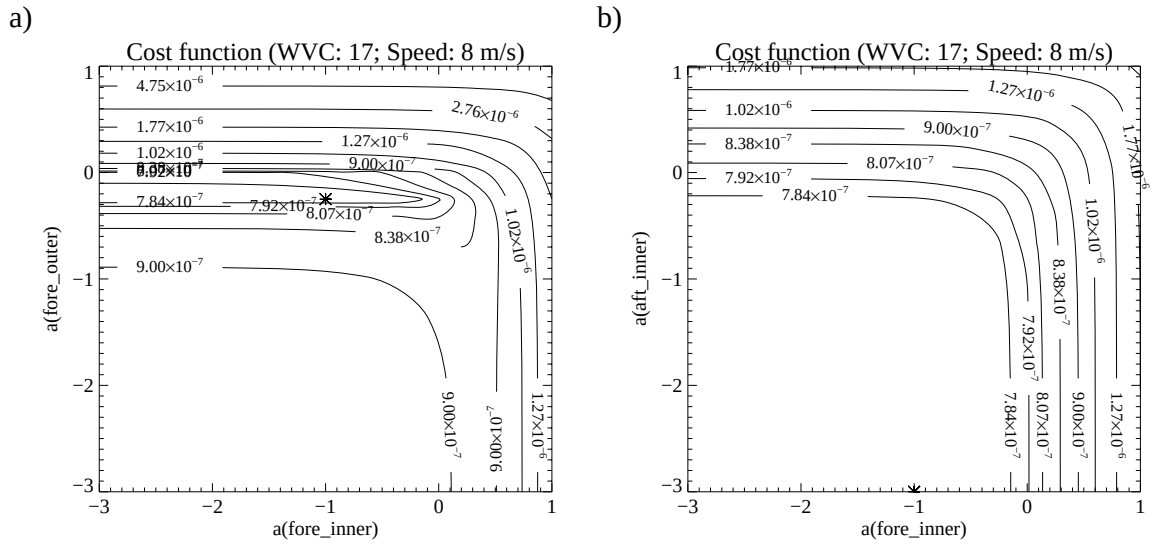

Figure 4.8 Contour plot of the four-dimensional cost function of the SeaWinds scaled sensitivities (see equation 4.6), corresponding to WVC number 17 and 8 m/s wind speed, for two different calibration coefficient plane cuts: (a) fore-inner / fore-outer; and (b) fore-inner / aft-inner. Such planes also contain the cost function minimum (star). The axes are in logarithmic scale (power of 10). The lowest contour line corresponds to a value 1% higher than the minimum.

Note the broad minimum in Figure 4.8a, indicating that, for a fore-outer coefficient value of about 0.6, any fore-inner coefficient value between 0.001 and 1 gives the same answer in the minimization. Figure 4.8b shows an even broader minimum compared to Figure 4.8a. In this case, any pair of fore-inner and aft-inner coefficient values between 0.001 and 0.6 gives the same answer in the minimization.

Similar to Figure 4.2, Figure 4.9 shows the histograms of the gradient of the total sensitivity curves from Figure 4.7, for non-calibrated (dotted lines) and calibrated (solid lines) sensitivities. As discussed in section 4.1.1, the distribution of gradients shows how flat the total sensitivity curve is, i.e., the lower the gradients are, the flatter the total sensitivity curve. As it is clearly discernible from the plots, the distributions are rather spread and show no accumulation around zero-gradient, denoting that the sensitivities are far from being flat. Moreover, the calibrated distributions (solid) are very similar to the non-calibrated ones (dotted), thus showing the poor effectiveness of the procedure.

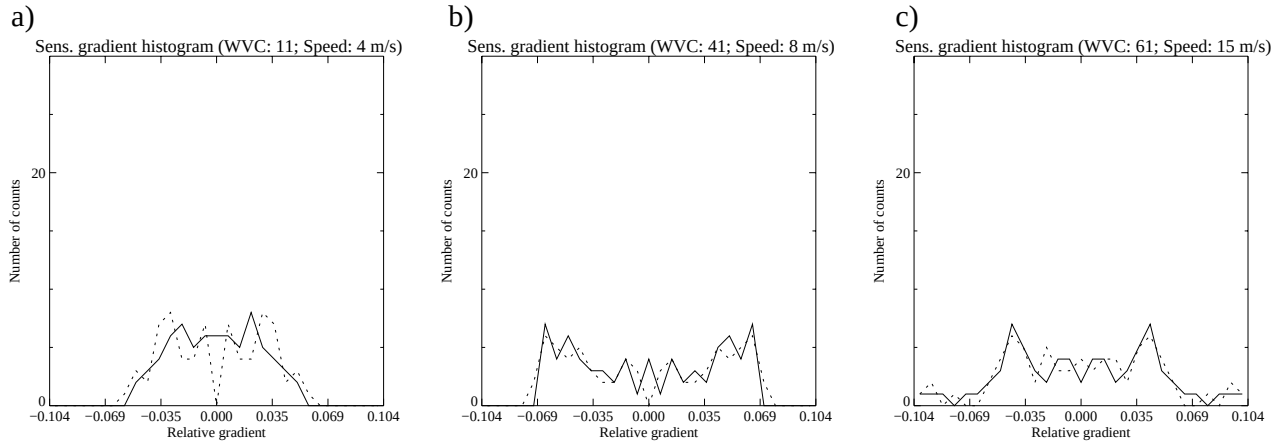

Figure 4.9 Histograms of the gradients of the total sensitivity curves from Figure 5.1, for a few WVC numbers and wind speed values: (a) WVC 11 and 4 m/s, (b) WVC 41 and 8 m/s, and (c) WVC 61 and 15 m/s. The gradient values are relative to the mean total sensitivity. The histograms correspond to non-calibrated (dotted) and calibrated (solid) sensitivities.

4.2.2 Wind direction performance

As discussed in section 4.2.1, the NSCAT-2 GMF total sensitivity as a function of wind direction is far from constant and the calibration does not effectively contribute in flattening the sensitivity curve. *Stoffelen and Anderson* (1997a) showed that, for ERS, the peaks and troughs of the total sensitivity curve are correlated with "artificial" (non-geophysically related) peaks and troughs in the retrieved wind direction distribution.

Figure 4.10 shows the total sensitivity as a function of WVC number and the retrieved wind direction (with respect to the satellite flight direction) for a wind speed of 8 m/s. The sensitivity values are plotted in grey scale. The sensitivity peaks (white) and troughs (black) shift as we move across the swath (i.e., with WVC number), drawing a pattern that is directly related to the beam relative geometry change across the swath. A very similar pattern is observed in the retrieved wind direction distributions shown by *Ebuchi* (1999), as such confirming the correlation between the sensitivity and the artificial accumulation of retrieved directions for SeaWinds as well.

In order to overcome the problem of the artificial accumulations, *Freilich et al* (2002) developed a new Ku-band GMF for SeaWinds on QuikSCAT, i.e., QSCAT-1. The latter was considerably removing the artificial wind direction accumulations. However, *Portabella and Stoffelen* (2002a) show that despite the artificial accumulations, NSCAT-2 GMF produces better quality winds than QSCAT-1 GMF. This shows that by tuning the GMF sensitivities to avoid such accumulations, one might end up with a modified GMF, which actually does not fit the measurements as well as the original GMF. The worse the fit is, the worse the wind retrieval.

In this study, we do not attempt to modify the GMF sensitivities but rather to manipulate (calibrate) the relative beam sensitivities in the inversion step such that no wind directions are favoured in the retrieval. The main difference is that we still use the best fit of the observations rather than an imperfect fit, therefore ensuring no harm in the wind retrieval quality. For ERS, the

calibration approach is effective. However, this is not the case for SeaWinds, since areas of "null" sensitivity exist.

As such, we conclude that for SeaWinds, there is no way to consistently remove the wind direction artificial accumulations without loss of wind retrieval accuracy. In terms of wind retrieval quality, it is best to use the GMF that best fits the observations. For latest developments on the sensitivity study, see Stoffelen and Portabella (2006).

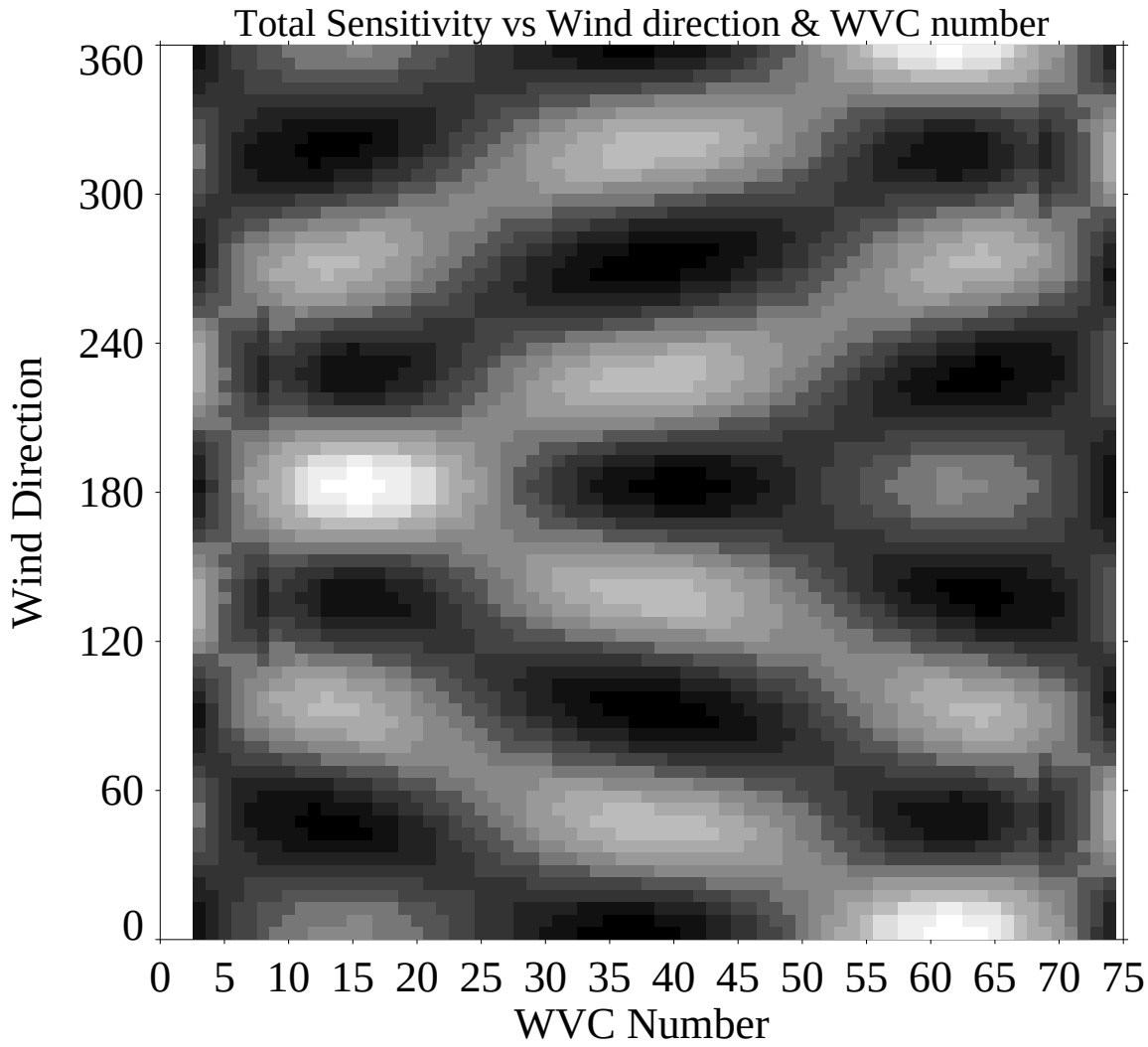

Figure 4.10 NSCAT-2 total sensitivity as a function of WVC number and retrieved wind direction, for a wind speed of 8 m/s. The sensitivity values are plotted in grey scale, ranging from black (troughs) to white (peaks).

5 Multiple Solutions

The MLE-based inversion has already been exhaustively revisited in section 4. The inversion procedure gives up to two (for ERS) and four (for SeaWinds) ambiguous wind solutions, which correspond to the MLE cost function minima (see equation 3.3).

In order to transfer the information content from inversion to the ambiguity removal (AR) scheme, a natural and effective step in scatterometry is to convert the MLE into a solution probability. As discussed in *Portabella* (2002), the probability of being the "true" wind given a set of scatterometer observations is related by definition (Gaussian noise assumption) to the MLE in the following way:

$$p(v \mid \sigma^o) \propto e^{-MLE/2}, \tag{5.1}$$

where v represents the "true" wind and σ^o the set of backscatter measurements. [Note that the integrated probability over the discrete number of ambiguous wind solutions is 1.] The theoretical relationship is therefore an exponential. In other words, as the MLE, which represents the misfit of the measurements with the solution lying on the GMF surface, increases, the probability of that particular solution being the "true" wind decreases exponentially. In reality, for several reasons such as the miscalculation of the measurement noise (see *Portabella, 2002*), the shape of the exponential may differ from the theory. A comprehensive characterization of the solution probability for SeaWinds, based on the empirical methodology described by *Stoffelen et al.* (2000) can be found in *Portabella and Stoffelen* (2002a). In this section, we repeat the same procedure for ERS.

5.1 ERS case

Following *Portabella and Stoffelen* (2002a), in order to assign probabilities for every wind solution, we first normalize the MLE and then use the method described by *Stoffelen et al.* (2000) to relate probabilities to the normalized MLE.

5.1.1 MLE normalization

The MLE represents a distance, which is "normalized" by the measurement error variance or noise (see equation 3.3). In this respect, the MLE should behave uniformly across the swath (WVC number) and over any wind condition, and its expectation value should be 1. However, this is not the case for SeaWinds, which often presents some unwanted dependencies, mainly

related to the misestimation of the measurement noise (a more detailed analysis on these dependencies can be found in section 2.4.3 of *Portabella, 2002*). In order to avoid this problem, for a given wind and WVC number, an expected MLE value can be estimated and used to normalize the MLE in the following way:

$$Rn = MLE / \langle MLE \rangle \quad (5.2)$$

where the <MLE> is the expected MLE and Rn the normalized MLE.

Since the noise model derived in section 3.1 is rather simple, a check on such MLE dependencies for ERS is needed prior to derive the wind solution probabilities. Figure 5.1 shows the mean MLE as a function of wind speed for different WVC numbers. We note that the mean MLE is rather constant with respect to wind speed for winds larger than 4 m/s, except for the most inner WVCs (see Figure 5.1a). For winds below 4 m/s, the mean MLE behaviour inside (solid) and outside (dashed) the cone is radically different. On the one hand, the mean MLE inside the cone decreases as the wind speed decreases, due to the truncation of the MLE distribution. That is, inside the cone, the range of distances between the triplets and the cone surface (MLE values) is limited to the actual size of the cone as the wind speed decreases, thus producing the mentioned truncation, which is enhanced as the cone cross-section decreases for decreasing wind speeds. On the other hand, the mean MLE outside the cone drastically increases as the wind speed decreases, denoting errors in the GMF. That is, the cone cross-sections are too small compared to the distributions of triplets (GMF misfit) and, as such, distances between the former and the latter (i.e., MLE) increase. Another indication of the mentioned GMF misfit is the fact that, for very low winds (below 3 m/s), the number of triplets outside the cone (dash-dotted) is substantially larger than the number of triplets inside the cone (dotted), even if larger numbers outside the cone are expected.

Despite the rather constant behaviour of the mean MLE as a function of wind speed (for winds above 4 m/s), a dependency on the WVC number is clearly discernible. The mean MLE varies from a value of about 1 at the outer swath (see Figure 5.1f) to a value of about 3 at the inner swath[1] (see Figure 5.1a). The results on the behaviour of the total Kp are in line with *Stoffelen and Anderson* (1997a). This suggests that we should correct for the measurement noise model derived in section 3, such that the total Kp increases with decreasing WVC number. As discussed in section 3.1.2, the geophysical noise increases with incidence angle, but incidence angle variations within the WVC were not considered here. If such variations reinforce the geophysical noise then, since the backscatter signal strongly increases with decreasing incidence angles (especially at low incidence angles), it produces a WVC-dependent increase in the noise level for decreasing WVC numbers. It is not clear though whether the substantial MLE increase observed (3 times larger in the inner than in the outer WVCs according to Figure 5.1) can be explained by this behaviour. A more detailed analysis on the Kp is therefore needed.

An alternative to modifying the Kp such that we obtain a more uniform MLE is actually to normalize the MLE at this stage. This simple procedure, successfully applied for SeaWinds (see *Portabella and Stoffelen, 2002a*) accounts for the Kp misestimations. The method consists of normalizing the MLE by the mean MLE values obtained (in this case) for every WVC number.

[1] Note that the MLE of figure 5.1 has not been normalized by the number of measurements (see equation 3.3). According to *Portabella and Stoffelen* (2002b), the expected MLE value will depend on the number of degrees of freedom of the noise in the measurement space. At the outer swath, where the noise is small compared to the cone diameter, the former has effectively one degree of freedom (perpendicular to the cone surface), and therefore the expected MLE value is 1. At the inner swath, where the noise is large compare to the cone diameter (especially at low winds), there can be at most two degrees of freedom, i.e., an expected MLE value of 2.

Because of the already discussed GMF errors and truncation problems, we should avoid winds below 4 m/s in the averaging, i.e. the MLE is not appropriate for noise estimation at such wind regime. The truncation problem however is present for winds below 8-10 m/s at the inner swath WVCs (see Figures 5.1a and 5.1b). As such, we exclude such winds for computing the mean or expected MLE used in the normalization (see equation 5.2).

5.1.2 Probability derivation

An empirical relationship between the probability of "true" wind and the MLE value for a given solution (inversion output) can be derived using only those cases which have exactly two solutions (i.e., two minima from equation 5.2) and ECMWF winds as reference (for more detailed information, see *Stoffelen et al., 2000*). Figure 5.2 shows the experimentally determined probability ratio of rank-2 Rn or Rn_2 (second deepest Rn minimum) and rank-1 Rn or Rn_1 (deepest Rn minimum) as a function of Rn_2 - Rn_1, for several values of Rn_1. Since Rn_1 is constant and therefore $p(Rn_1)$ is also constant, this plot is actually showing the shape of the relationship between probability and Rn. The solid line, which represents the exponential of equation 5.1 (note that Rn is used instead of MLE), fits very well the experimentally determined probability for the overall data (see Figure 5.2a), denoting a good agreement between theory and real data. However, if we compare such probabilities by swath region, we see that for the outer swath (Figure 5.2d), there is a misfit between experimental and theoretical probabilities, especially for low Rn differences, where there is a clear underestimation of the former compared to the latter. A 10%-20% misfit in probability ratio corresponds, for ERS (only two solutions), in a rank-1 probability misfit below 10%. Such anomalous behavior (at the outer swath) needs further investigation.

In order to further quantify the misfit between experimental and theoretical probabilities, we use the theoretical function (equation 5.1) to predict how often a certain solution rank corresponds to the "true" solution. Table 5.1 compares the "predicted" distributions with the "observed" distributions (using the closest to ECMWF) over the different ranks (note that for ERS we almost always get two solutions from inversion, and therefore only this case is shown in the table) for different parts of the swath. As expected, the disagreement between the theoretical and the experimental probabilities is maximal (7%) at the outer swath.

Table 5.1 Predicted / observed distributions

	All swath	Inner Swath	Mid Swath	Outer Swath
Number of Data	2966085	970039	1096052	899994
Rank 1 (%)	63 / 65	64 / 62	62 / 64	62 / 69
Rank 2 (%)	37 / 35	36 / 38	38 / 36	38 / 31

It is also important to discuss the behavior of the experimentally derived probability for winds below 4 m/s. Such probability is very close to 1 for any Rn_2 - Rn_1 value (not shown) and therefore does not behave at all as the theoretical exponential. This indicates no skill in the inversion solutions, i.e., equally likely solutions. No significant skill differences are seen when comparing different swath regions. In other words, the results show that for low winds, the wind direction sensitivity[1] is small compared to the noise. As such, equal probabilities are assigned to the wind solutions for winds below 4 m/s.

In summary, we show a way to experimentally derive the relationship between probability and MLE. This relationship is very close to the theoretical exponential (except for low winds) both for ERS and SeaWinds (*Portabella and Stoffelen, 2002a,* found a similar exponential with 1.4, instead of 2, in the exponent denominator of equation 5.1), suggesting that once the MLE is consistently normalized, equation 5.1 can be used for any type of scatterometer.

[1] Note that for ERS, the wind solutions have very similar wind speed values and therefore the main difference between rank-1 and rank-2 solutions is given by the wind direction.

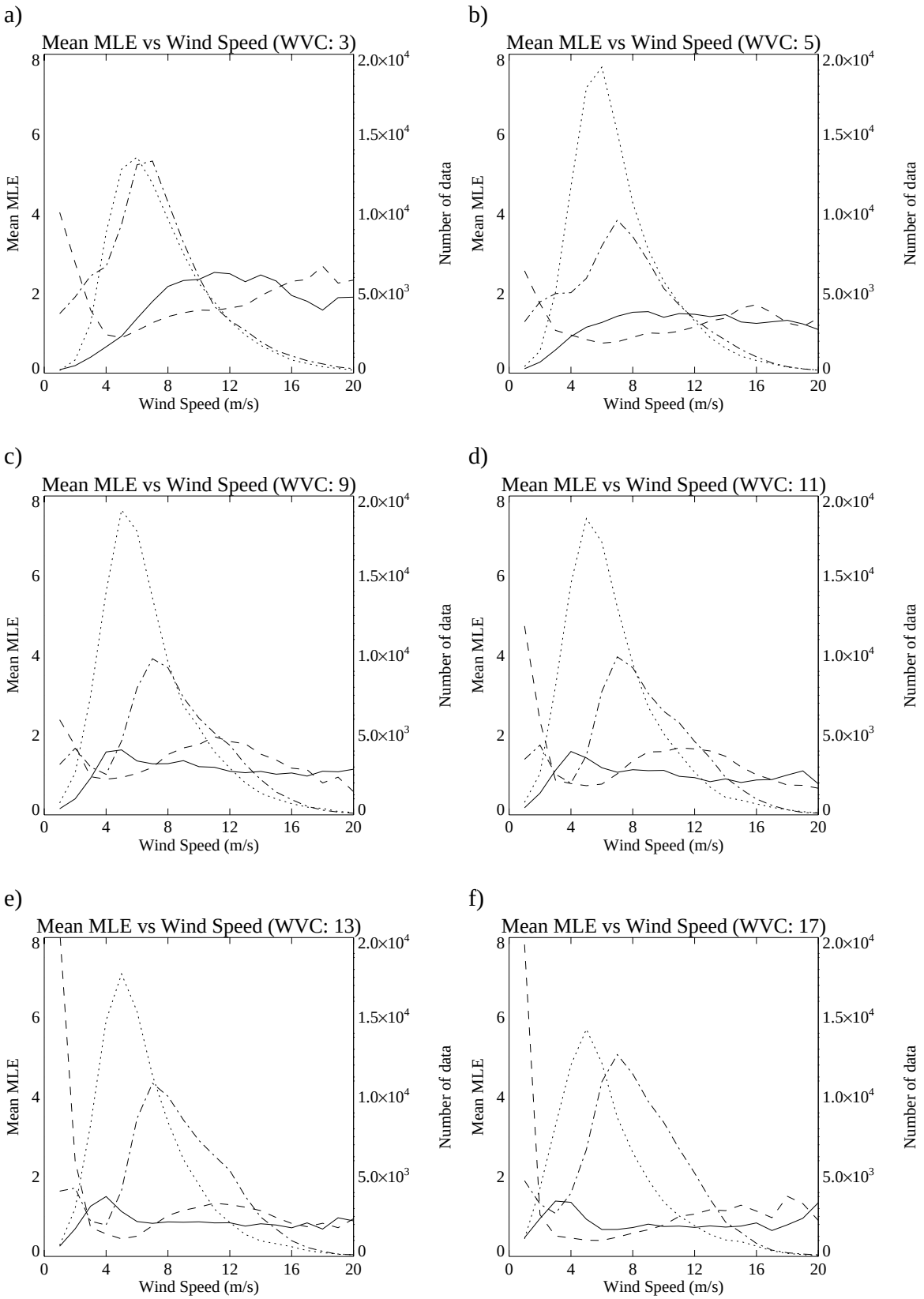

Figure 5.1 Mean MLE as a function of wind speed for ERS triplets inside (solid) and outside (dashed) the cone, and for WVC numbers 3 (a), 5 (b), 9 (c), 11 (d), 13 (e), and 17 (f). The number of triplets used in the mean computation, inside (dotted) and outside (dash-dotted) the cone, is also plotted.

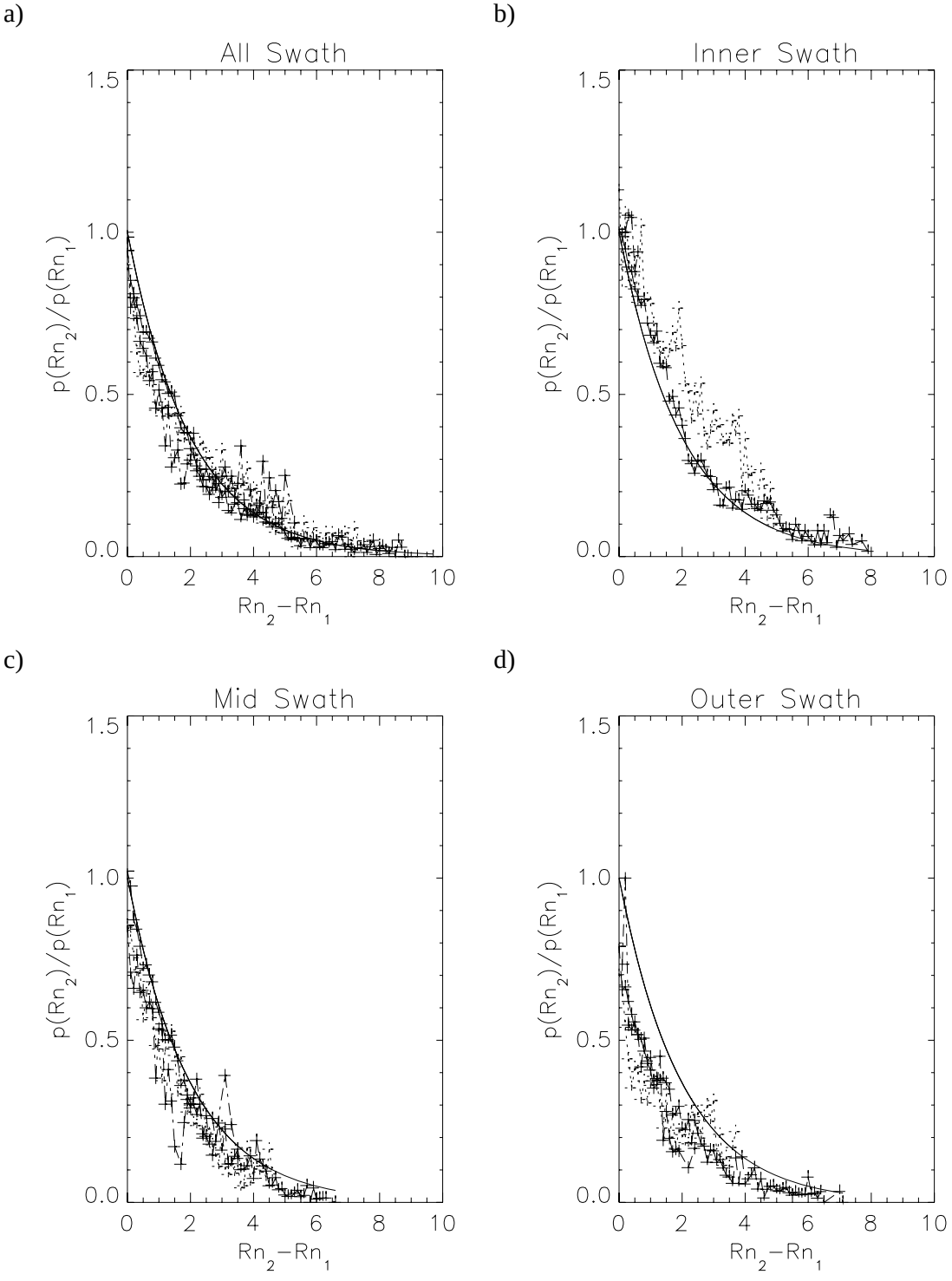

Figure 5.2 Ratio of the number of realizations of Rn_2 and the number of realizations of Rn_1 as a function of Rn_2-Rn_1, and values of Rn_1=0.1 (dotted), Rn1.=1.1 (dashed), and Rn_1=2.4 (dash-dotted). The solid line represents the exponential of equation 5.1. Plot a represents the entire swath; plot b, the inner swath (WVC numbers 1-6); plot c, the mid swath (WVC numbers 7-13); and plot d, the outer swath (WVC numbers 14-19).

6 Conclusions and future work

A software has been developed to generate a database of collocated scatterometer (i.e., ERS and SeaWinds) and ECMWF-reanalysis winds. The software is using the Binary Universal Format Representation (BUFR) for input and output. In this respect, NSCAT data were never distributed in BUFR. As such, only ERS and SeaWinds scatterometer data are included in the database. The exclusion of NSCAT from the database is however not very relevant since its main characteristics are already present either in ERS or in SeaWinds, e.g. fixed antennae (ERS), dual-polarization (SeaWinds), Ku-band (SeaWinds).

The wind retrieval problem for ERS is revisited in this project. In contrast with NSCAT and SeaWinds, ERS uses no *Kp* normalization in the MLE inversion to optimize wind retrieval. As a first attempt to find a generic wind retrieval method that is suitable for all scatterometer systems and therefore useful for FoM, the *Kp* normalization is tested for ERS.

For such purpose, a geophysical noise model is needed. Through visualization of the 3D measurement space, real triplets are compared to simulated triplets for different geophysical noise parameter values. Then, the parameters that better represent the real triplet distributions are selected and used for computing the geophysical noise model. The simulations well reproduce the real data and, as such, validate the derived geophysical noise model for different WVC numbers and wind speeds.

Despite the successful derivation of the geophysical noise, the *Kp* normalization produces unsatisfactory results in terms of MLE inversion, i.e. the resulting cone shape becomes rather elliptic thus reducing the wind retrieval quality. We therefore confirm that the shape of the cone is more important than the noise properties for wind retrieval.

Stoffelen and Anderson (1997a) show that by using no Kp normalisation in the MLE inversion and by transforming the measurement space, the cone shape becomes circular and the wind retrieval improves. Since it is important to come up with a generic wind retrieval method, it seems reasonable now to test such approach for NSCAT and SeaWinds.

For ERS, the transformation could be analytically derived, since the measurement space is 3-dimensional. However, repeating this exercise for NSCAT or QuikSCAT is not straightforward as their measurement space is 4-dimensional. We therefore propose a generic method that seeks for the best measurement space transformation in a numerical way. Since the transformation is already performed for ERS, we can use the latter to validate the proposed method and later apply it to SeaWinds and/or NSCAT.

The calibration method consists of making the total sensitivity (with respect to wind direction) as constant as possible, i.e., the ERS cone as circular as possible, by calibrating the individual beam sensitivities. As such, for every wind speed and WVC number, a set of calibration coefficients is found by minimizing the (squared) distance between the total sensitivity curve and its mean value.

The calibration procedure is most effective, in terms of producing a more circular cone, at the inner swath (WVC numbers 1 to 6), especially for low and moderate winds, and least effective for high winds and outer regions (WVC numbers 13 to 19).

We validate the calibration against ECMWF winds, using as a reference the z space and the non-calibrated (Kp norm) inversions. In terms of wind component errors, the three inversion types show similar scores when compared to ECMWF. However, we note some differences in the wind direction domain. Although the highest wind direction skill corresponds to the z-space inversion, the calibration shows improvement with respect to Kp norm, especially in the inner swath where its skill is similar to the z space skill. As such, the calibration method turns out to be a good alternative to the z-space inversion, and since it is generic for scatterometer systems, we now test it for SeaWinds.

The calibration turns out to be little effective for SeaWinds. This is mainly due to the relative geometry of the SeaWinds beams and to the behaviour of the wind direction sensitivity of the H-pol beams. Certain wind directions show almost no sensitivity for any given beam, thus making the calibration of the individual beam sensitivities little effective.

The correlation between the peaks and troughs of the total sensitivity and the artificial (non-geophysically related) accumulations of the retrieved wind direction distribution is discussed. Alternatives to remove such accumulations are also discussed. It turns out that by tuning the GMF sensitivities to avoid the accumulations, the GMF is modified and does not represent anymore the best fit of the observations. As such, the wind retrieval quality is decreased. Consequently, for wind retrieval, it is best to use the GMF that represents the best fit of the observations, despite the artificial accumulations in the retrieved wind direction distribution.

The empirical method used by *Portabella and Stoffelen* (2002a) to determine the relationship between the probability of a certain wind solution (inversion output) of being the “true” wind and its MLE value for SeaWinds is used here for ERS.

For such purpose, MLE dependencies on wind speed and WVC number are checked. The results reveal some errors in the GMF at low winds as well as the truncation of the MLE distributions for triplets located inside the cone. An MLE dependency on the WVC number is also shown, denoting a misestimation of the noise, which increases with decreasing WVC number. A combination of wind variability and incidence angle variability may be the cause, but further investigation is required. To circumvent this problem, the MLE is normalized. As such, the MLE that is most appropriate for the noise estimation (i.e., corresponding to moderate and high winds) is averaged per WVC number and used as normalization factor.

The normalized MLE (Rn) is then used in the empirical derivation of the probability. Rank-1 and rank-2 Rn data together with ECMWF wind data (as reference) are used. Similar to SeaWinds, the experimental probability for ERS is in agreement with the theoretical one. Some disagreement is found at the outer swath regions (of ERS) for low Rn values, which needs further investigation.

The general agreement between experimental and theoretical probabilities suggests that the theoretical function can be used for any past, current or future scatterometer system, provided that the MLE is normalized, i.e., the backscatter noise is known.

Appendix A

As discussed in section 4.1.1, for every wind speed and WVC number, equation 4.6 is minimized and a set of calibration coefficients (a_1,a_2,a_3) is found. As a result of the minimization, we produce a calibration coefficient table for wind speeds ranging from 1 m/s to 20 m/s (bins of 1 m/s) and WVC numbers ranging from 1 to 19. For wind speeds lower than 1 m/s and higher than 20 m/s, we use the calibration coefficients corresponding to 1 m/s and 20 m/s, respectively.

Figure A.1 and A.2 show the calibration coefficients as a function of wind speed for every odd WVC number.

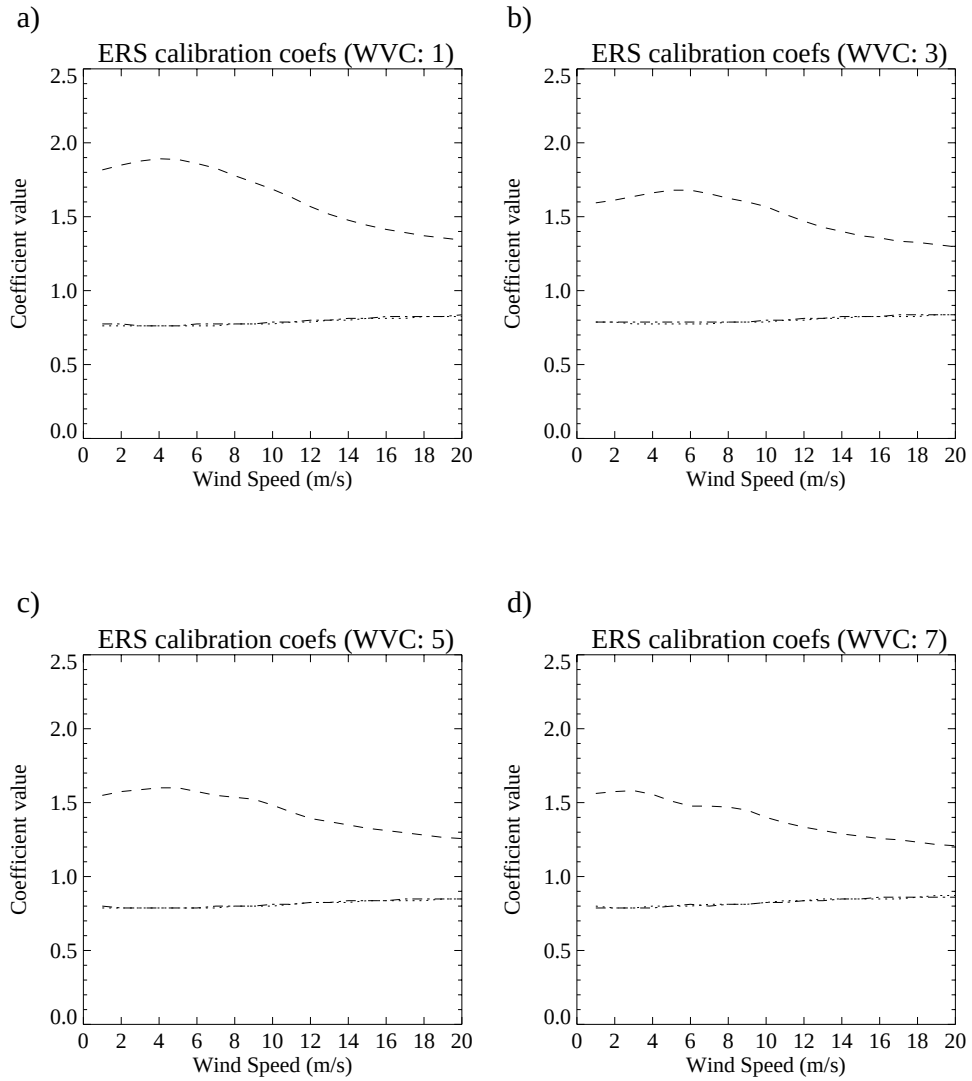

Figure A.1 a1 (dotted), a2 (dashed), and a3 (dash-dotted) calibration coefficients as a function of wind speed for WVC numbers 1 (a), 3 (b), 5 (c), and 7 (d).

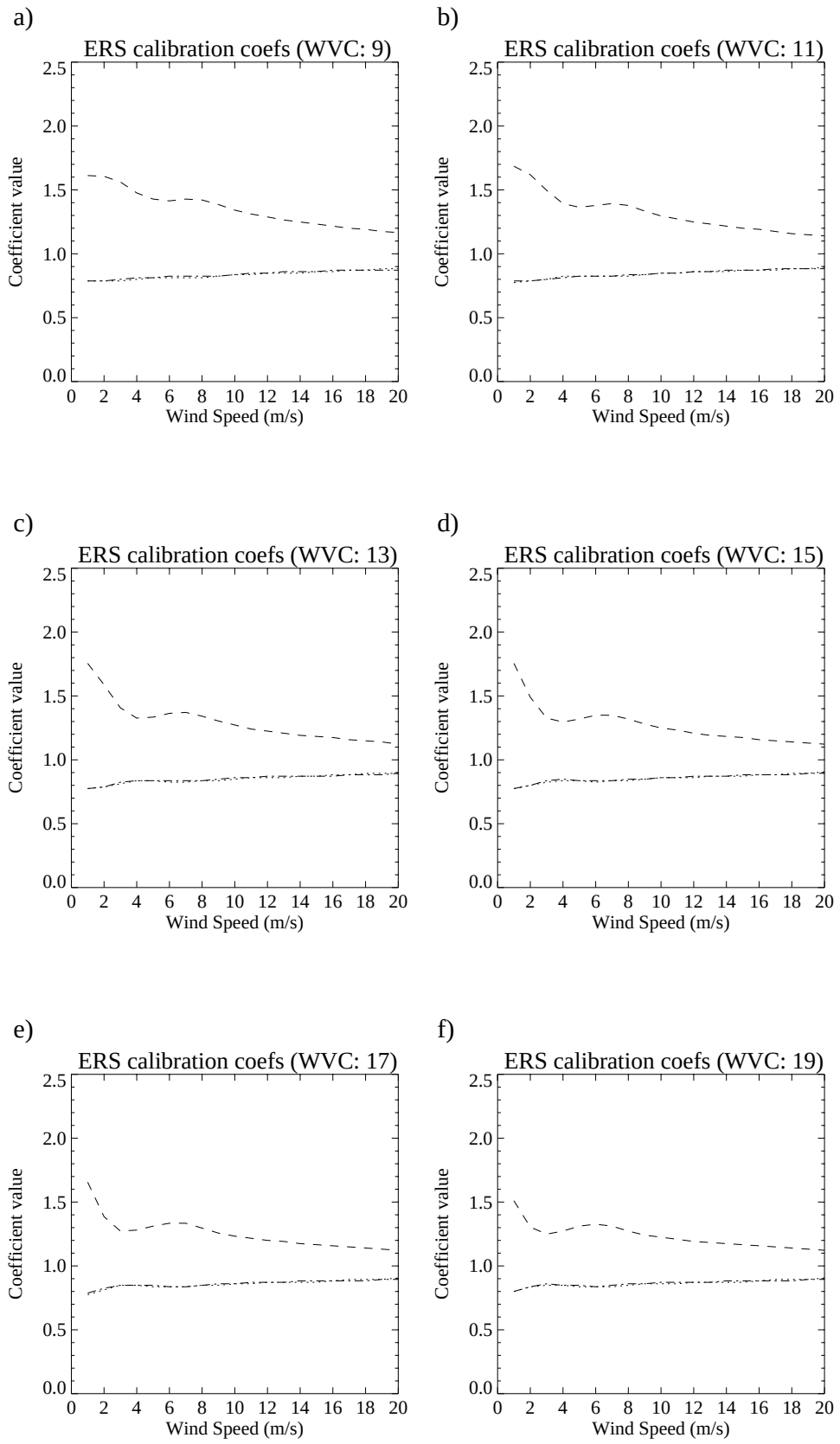

Figure A.2 Same as Figure A.1 but for WVC numbers 9 (a), 11 (b), 13 (c), 15 (d), 17 (e), and 19 (f).

References

Ebuchi, N., "Statistical distribution of wind directions observed by QSCAT," *Proc. of fisrt QuikSCAT Cal/Val Workshop*, Pasadena/Arcadia (USA), 1999.

Freilich, M.H., Vanhoff, B.A., and Dunbar, R.S., "Empirical determination of a Ku-band wind model function from SeaWinds scanning scatterometer," *J. Geophys. Res.* (in prep.), 2002.

Graham, R., Anderson, D., Hollingsworth, A., and Böttger, H., Evaluation of ERS-1 wind extraction and ambiguity removal algorithms: meteorological and statistical evaluation," *ECMWF report*, ECMWF, Reading, United Kingdom, 1989.

Hersbach, H., "CMOD-5: an improved geophysical model function for ERS C-band scatterometry," *Technical Memorandum*, no. 395, ECMWF, Reading, United Kingdom, 2003.

JPL, "QuikSCAT science data product user's manual," version 2.2, *Jet Propulsion Laboratory D-12985*, pp. 89, December 2001.

Portabella, M., and Stoffelen, A., "Rain detection and quality control of SeaWinds," *J. Atm. and Ocean Techn*., vol. 18, no. 7, pp. 1171-1183, 2001.

Portabella, M., "Wind field retrieval from satellite radar systems," *PhD thesis at the University of Barcelona*, ISBN 90-6464-499-3, September 2002.

Portabella, M., and Stoffelen, A., "Quality control and wind retrieval for SeaWinds," *Scientific report WR-2002-01*, Koninklijk Nederlands Meteorologisch Instituut, The Netherlands, 2002a.

Portabella, M., and Stoffelen, A., "Characterization of residual information for SeaWinds quality control," *IEEE Trans. Geosci. Rem. Sens.*, vol. 40, no. 12, pp. 2747-2759, 2002b.

Portabella, M., and Stoffelen, A., "Scatterometer backscatter uncertainty due to wind variability," submitted to *IEEE Trans. Geosci. Rem. Sens.*, September 2005.

Stoffelen, A., and Anderson D., "Scatterometer data interpretation: measurement space and inversion," *J. Atm. and Ocean. Techn*., vol. 14(6), pp. 1298-1313, 1997a.

Stoffelen, A., and Anderson, D., "Scatterometer data interpretation: derivation of the transfer function CMOD-4," *J. Geophys. Res.*, vol. 102, no. C3, pp. 5767-5780, 1997b.

Stoffelen, A., "Scatterometry," *PhD thesis at the University of Utrecht*, ISBN 90-393-1708-9, October 1998.

Stoffelen, A., and Portabella, M., "On Bayesian scatterometer wind inversion," *IEEE Trans. Geosci. Rem. Sens.*, in press, 2006.

Wentz, F.J., and Smith, D.K., "A model function for the ocean normalized radar cross section at 14 GHz derived from NSCAT observations," *J. Geophys. Res*., vol. 104, C5, pp. 11499-11514, 1999.